Soft Science

Review Article

Portable green energy out of the blue: hydrogel-based energy conversion devices

Chang Liu[1],#, Sijia Wang[2],#, Shien-Ping Feng[2,3],*, Nicholas X. Fang[1,2],*

[1]Department of Mechanical Engineering, Massachusetts Institute of Technology, Cambridge, MA 02139, USA.
[2]Department of Mechanical Engineering, The University of Hong Kong, Hong Kong 999077, China.
[3]Department of Advanced Design and Systems Engineering, City University of Hong Kong, Hong Kong, China.
#Authors contributed equally.

*Correspondence to:** Prof. Shien-Ping Feng, Department of Mechanical Engineering, The University of Hong Kong, Pokfulam Road, Hong Kong 999077, China; Department of Advanced Design and Systems Engineering, City University of Hong Kong, Kowloon, Hong Kong. China. E-mail: tony.feng@cityu.edu.hk; Prof. Nicholas X. Fang, Department of Mechanical Engineering, Massachusetts Institute of Technology, Cambridge, MA 02139, USA; Department of Mechanical Engineering, The University of Hong Kong, Pokfulam Road, Hong Kong 999077, China. E-mail: nicfang@mit.edu

Abstract

To alleviate the escalating global demands for electricity with a low carbon footprint, we can resort to a green energy source that is conveyed by tiny temperature or moisture gradients. A tremendous source of low-grade energy scatters around us and remains unutilized, which is why thermoelectric and hydrovoltaic devices were invented. Our review focuses on a growing trend of implementing hydrogel-based ionic thermoelectric systems and hydrovoltaic devices as they hold the promise of electric outputs that are several times higher than conventional solid-state inorganic counterparts. This is due to the molecular-level tailorable features of hydrogel polymers and their interactions with water and other functional additives, which provide an ideal platform for low-grade heat and water energy harvesting from fundamental and practical perspectives. This review is divided into three sections. We present working principles, engineering concepts, state-of-art designs, and urgent challenges for hydrogel-based (i) ionic thermoelectric systems; (ii) hydrovoltaic devices; and (iii) their hybrids.

Keywords: Low-grade heat, ionic thermoelectric, hydrovoltaic energy, hydrogel, power generation

INTRODUCTION

Two of the biggest challenges of the 21st century at the global level are the energy crisis and climate change issues[1]. To address the increasing worldwide demand for electricity without added carbon emission, energy recovery systems that capitalize on the low-grade energy in terms of low-grade heat or water for direct electricity production offer a promising strategy, especially of which low-grade heat and water (e.g., moisture, droplets) share the same significant advantages of omnipresence and abundance in our living environment. Envision this scenario: the low-grade waste heat ejected by air conditioners is emitted to the outdoors; meanwhile, the indoor humidity is reduced by running air conditioners compared with humid outdoors in the places like Singapore, Hong Kong, New Orleans, *etc*. Thus, temperature and moisture gradients are built across indoor and outdoor environments and offer a great opportunity for electricity production [Figure 1]. Likewise, our bodies generate a similar temperature gradient or moisture gradient towards the surrounding environment, making easy access to such energy sources with the prospect of power generation.

Any kind of gradient is equivalent to a driving force that could do work in the system. Conventional electrochemical energy conversion systems have been developed with proven utility and ability to harvest the scattered energy in the environment. This provides us with significant experience in paring electrodes, electrolytes, separators, *etc*., to optimize these systems from the mechanism, design, and energy conversion efficiency. Particularly, a small difference in temperature or moisture can lead to a reaction entropy change or chemical potential change in an electrochemical system[2,3]. Access to such gradient sources is very appealing for extensive energy recovery and portable power supply. With the aid of gelation chemistry to build a quasi-solid-state device without moving fluids, there is a growing trend of using hydrogel materials to upgrade electric outputs in new ionic thermoelectric systems (i-TEs) and hydrovoltaic devices [Figure 2].

Hydrogel is a three-dimensional (3D) network of hydrophilic polymers from cross-linked individual polymer chains, which can swell and hold large amounts of water while maintaining a defined structure[4]. Taking advantage of multitudinous and tunable molecular building blocks and rational integration with functional additives such as redox couples, salts, ligands, and secondary polymers [Figure 3A], not only can hydrogels enable water absorption and retention properties and desirable features of transport of mass and ion but also provide large surface areas for active sites and abundant pendant groups for versatile function[5]. These properties underpin their applications in i-TEs and hydrovoltaic devices, where hydrogels have been used as local concentration regulators, polyelectrolytes, transport media, separators, ion channels, surface functional layers, and many more [Figure 3B][6-10]. Despite microcosmic pictures of ion transport in bulk hydrogel or interfacial redox processes remaining to be explored, they are important for us to obtain fundamental insights and optimize macroscopic properties and performance. Generally, hydrogel-based i-TEs and hydrovoltaic devices are operated separately, whereas, as the heat gain (or loss) and corresponding temperature regulations are naturally correlated with the events of water in hydrogels (e.g., condensation, convection, evaporation), the hydrogel component in the one (hydrovoltaic device) can work jointly with the other (i-TE), and vice versa for maintaining the temperature gradient or enhancing water evaporation[10,11] Such synergies between temperature gradient and transpiration induced charge concentration at the electrode interface may be exploited for increasing output voltage [Figure 2].

In this review, we summarize the fundamental mechanisms and engineering concepts related to the development of hydrogel-based i-TEs, hydrovoltaic devices, and their hybrids. We highlight the similarities in working principles between i-TEs and hydrovoltaic devices and the opportunities for the discharge modes of the former to be extended and adopted by the latter to improve power output. In each session, we start with working mechanisms, then present recent progress in how hydrogel materials were integrated
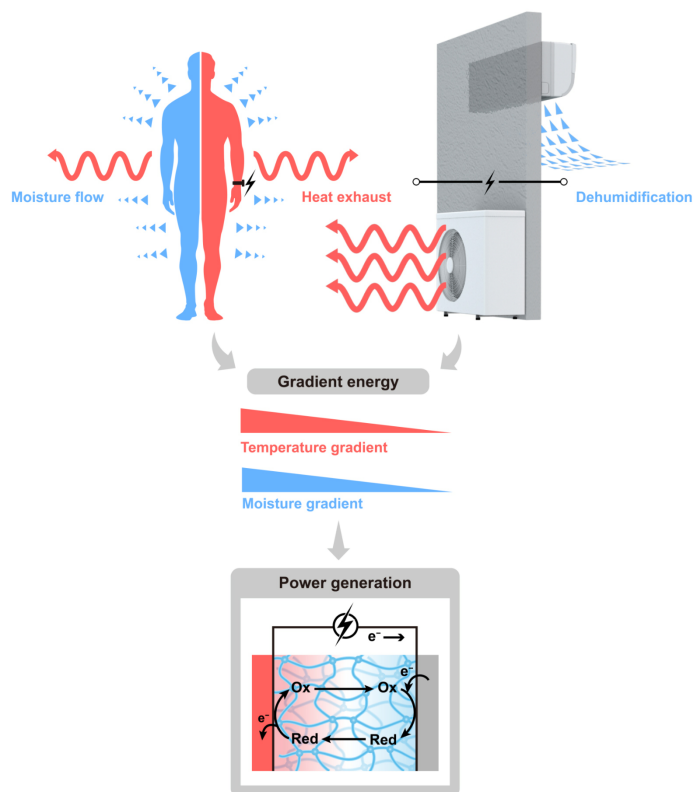
Figure 1. Two examples of low-grade energy of moisture and low-grade heat co-existing in our living environment. Body heat and moisture from breathing, sweating, cutaneous transpiration, *etc.*, can be harnessed for power generation based on hydrogel materials. Exhaust heat from air conditioners and relative humidity differences between indoor and outdoor environments can also be utilized to produce electricity through hydrogel materials. (Ionic species at oxidized state and reduced state are expressed as Ox and Red, respectively).
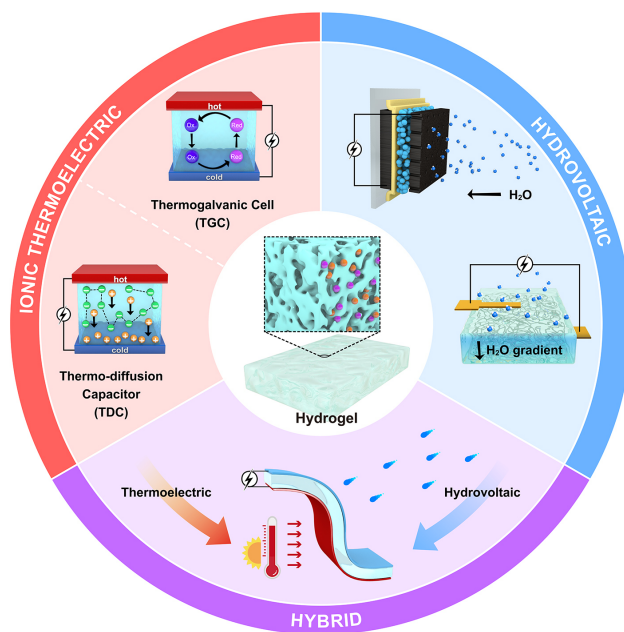
Figure 2. The scope of the present review including hydrogel-based ionic thermoelectric systems, hydrovoltaic devices, and their hybrids.
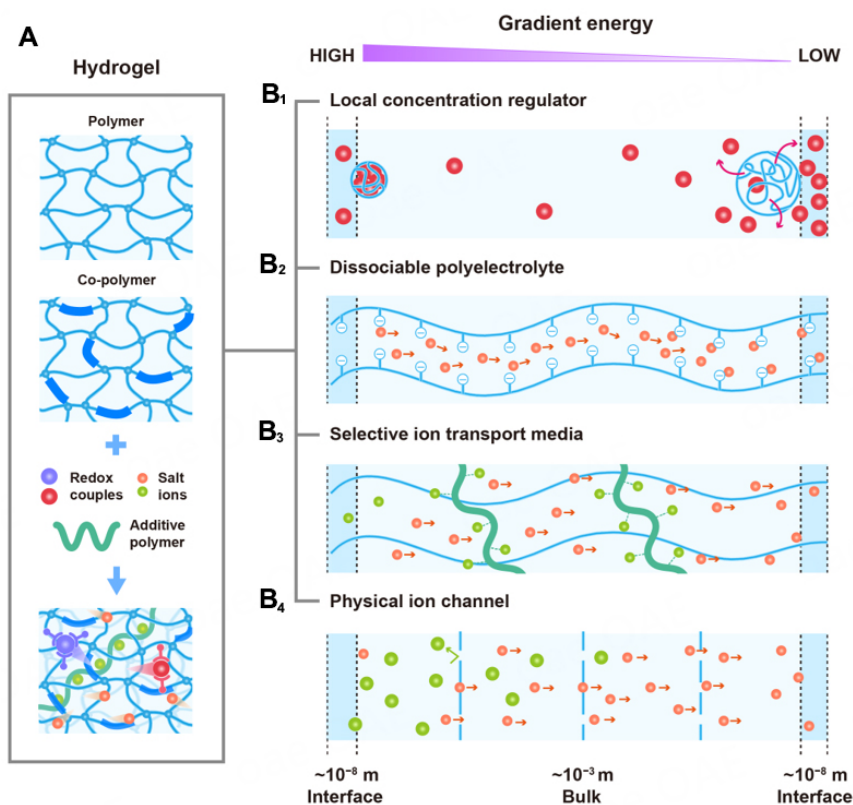
Figure 3. (A) Hydrogel network and functional additives including redox couples, salt ions, and additive polymers. (B) General routes of utilizing gradient energy with the aid of hydrogel materials. (B_1) Phase-change hydrogel serves as a local concentration regulator to suppress or promote redox reactions at the electrode and electrolyte interfaces. (B_2) Either dry polyelectrolyte adsorbing water from moist air or wet polyelectrolyte being thermally activated can release charged mobile ions to establish a concentration gradient across the hydrogel. (B_3) Introduction of functional additives into the hydrogel can selectively localize anions but facilitate the ions with the opposite charge, consequently building the concentration gradient. (B_4) Hydrogel made of nano/microchannels (or designed physical constraints) works as an ion-selective membrane. In (B_1-B_4) the hydrogel performs in different length scales (i.e., at the interface or in bulk).

with those energy conversion systems, and conclude with remaining challenges involving unknown mechanisms, future practical applications, and perspectives.

IONIC THERMOELECTRIC SYSTEMS USING HYDROGEL MATERIALS

Abundant sources of waste heat exist in many industries and daily life due to limitations of current power generation technologies; approximately 60% is in the form of low-grade heat (< 100 °C)[12]. Especially considering the environmental energy capture, the applicable temperature window is further narrowed down to ~15 °C (e.g., the human body of 37 °C to the surroundings of 22 °C). Conventional solid-state thermoelectric materials (TEs), including semiconductors and conducting polymers, were expected to be a prioritized solution to regenerate energy from waste heat and supply electric power through asymmetric electron (or hole) distribution and transport of the generated charge carriers in n-type (or p-type) TEs driven by a temperature gradient [Figure 4A]. Because of the small thermopower of approximately 100-200 $\mu V\ K^{-1}$, to meet a practical voltage of 1-5 V, we need to keep tremendous temperature gradients or connect thousands of TE units in tandem, or through a voltage amplifier[13,14]. Recent developments in i-TEs extend the applicable temperature window to low-grade heat and show potential for pragmatic daily applications by virtue of very high thermal sensitivities (i.e., thermopower up to tens of $mV\ K^{-1}$)[15-18].
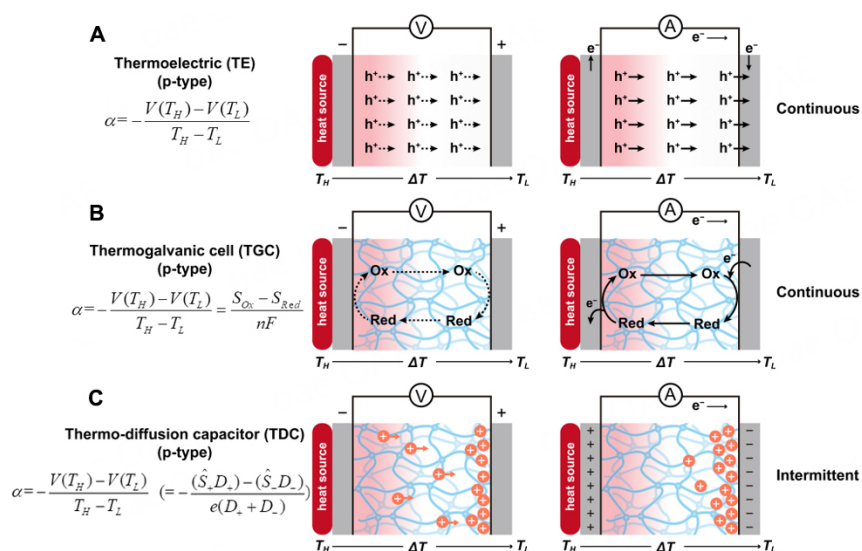
Figure 4. Working mechanism of TE, TGC and TDC. (A) A p-type TE with continuous hole flow driven by a temperature gradient. α is the thermopower, ΔV and ΔT are the potential difference and temperature difference between the hot and cold electrodes, respectively. $V(T_H)$, $V(T_L)$, T_H and T_L represent the potential and temperature at the hot and cold electrodes, respectively. (B) A p-type TGC with a redox reaction $Ox + ne^- \leftrightarrow Red$, producing a continuous current with electrochemical reactions occurring at the hot and cold electrodes. n is the number of electrons transferred in the reaction, F is the faradic constant, S_{ox} and S_{red} are the molar entropy of the redox species. (C) A p-type TDC with cations diffusing with higher mobility over anions, producing an intermittent current through the thermal charging and electrical discharging cycle. $\hat{S}$ is the Eastman entropy and D is ion diffusion coefficient. Note that the equation used to estimate the thermopower of TDCs is a theoretical example, which is derived from the simple system, e.g., a KCl aqueous electrolyte at ideal conditions.

Among various i-TEs for low-grade heat-to-electricity conversion, two technical routes have drawn extensive attention, namely, thermogalvanic cells (TGCs) and thermo-diffusion capacitors (TDCs). TGCs have a relatively long history which dates back to the late 1970s when Burrow[19] and Quickenden[20,21] proposed liquid-based alternatives to solid TEs. A typical TGC works under a thermal gradient, with redox reactions occurring at two electrodes to produce a steady current through the external circuit [Figure 4B]. TGCs, leveraging temperature-dependent redox reactions on spatial or time scales, have inspired several auspicious derivatives, such as thermal regenerative cycles (TRECs)[22-28], thermal regenerative ammonia-based batteries (TRABs)[29,30], CO_2-induced pH-sensitive thermally regenerative cells (pH-TRCs)[31,32], direct thermal charging cells (DTCCs)[33,34], and more. In contrast, a typical TDC converts heat to electric power based on thermal-induced ion diffusion and is operated like a (super)capacitor to transduce an ion concentration gradient in the electrolyte to the electron flow through the external circuit [Figure 4C]. Both TGCs and TDCs containing redox couples or salt ions fundamentally differ from TEs, in which electrons and holes can directly pass through the electrodes [Figure 4A]. Interfacial reactions (for TGCs) or ions accumulation (for TDCs) occurring at a very small distance from electrode surfaces (within tens of nanometers that are deduced from EDLs) dominate the thermoelectric response in terms of magnitude and speed[35]. Therefore, i-TEs are required to be "electrically thin" to ensure fast kinetics but "thermally thick" to maintain a proper temperature difference.

Various i-TEs have distinct origins of technology; the indicator used to describe thermoelectric performance (e.g., Seebeck coefficient and temperature coefficient) varies from work to work. To be more precise and comparable, the thermopower (α) is defined here with the same expression:

$$\alpha = -\frac{\Delta V}{\Delta T} = -\frac{V(T_H) - V(T_L)}{T_H - T_L} \qquad (1)$$

where ΔV and ΔT are the potential difference and temperature difference between the hot and cold electrodes. $V(T_H)$, $V(T_L)$, T_H, and T_L represent the potential and temperature on the hot and cold electrodes, respectively. In analogy with solid-state TEs, a system with a positive α will be called "p-type" while the negative α will be called "n-type" in the following discussion.

Biological hydrogels that can convert thermal stimulus into electric signals have been discovered in sharks, and thermoelectric heat pumps exist in wasps[36,37], which suggests the great potential of hydrogel materials to be adopted by i-TEs. A large and growing body of research endeavors has been devoted to hydrogel-based i-TEs, where the interactions among electrodes, ions, and solvent-rich media govern the working mechanisms involving a faradic effect, non-faradic effect, or synergistic effect. As a highly solvent-rich and customizable material, hydrogel exhibits versatile features and exceptional adaptabilities that match well with i-TEs[5,38]. First, benefiting from gelation chemistry, hydrogels can be well integrated into electrodes, polyelectrolytes (with redox couples or non-redox active ionic species), ion channels, and more. Second, a solvent-rich environment permits sufficient ion dissociation and ion transport[5]. Third, the polymer matrix minimizes convective heat transfer in the electrolytes to maintain the temperature gradient for long-term operation. Moreover, an additional benefit for hydrogel-based i-TEs is the ease of serial connections of n-p units to increase the voltage and current output[39]. Other general advantages of hydrogel materials, such as softness and stretchability[8,40,41], self-healing[42], *etc.*, have also been integrated into a variety of i-TEs.

Hydrogels in thermogalvanic cells

In TGCs, a thin layer of electrolyte containing redox couples is sandwiched by hot and cold electrodes [Figure 4B]. The reaction entropy of the redox couple is sensitive to the local temperature. Ions are oxidized or reduced at electrolyte-electrode interfaces to produce electricity continuously. For a redox reaction $Ox + ne^- \leftrightarrow Red$, the thermopower is $\alpha = -\frac{V(T_H) - V(T_L)}{T_H - T_L} == -\alpha_r = -\frac{\Delta S_r}{nF}$, $\Delta S_r = S_{Red} - S_{Ox}$, where α_r is the thermogalvanic coefficient (also known as temperature coefficient), n is the number of transferred electrons of the reaction, F is the faradic constant, ΔS_r is the reaction entropy change, S_{ox} and S_{red} are the molar entropy of the redox species[3]. The rational choice of a redox couple is essential to fabricate a high-performance TGC, and, ideally, a large reaction entropy dictates a large thermopower. Extensive research has focused on finding superior redox couples such as ferri/ferrocyanide ($Fe(CN)_6^{3-}/Fe(CN)_6^{4-}$)[43-46], ferrous/ferric (Fe^{2+}/Fe^{3+})[46-48], iodide/triiodide (I^-/I_3^-)[44], vanadium (V^{2+}/V^{3+})[46], cobalt complex ($Co(bpy)_3^{2+}/Co(bpy)_3^{3+}$)[49], *etc.* [Table 1]. Their thermopowers change in response to varying ion concentrations, pH, additives, *etc.* In addition to soluble redox couples, some solid-state electrode materials that are dissolved/redeposited at electrodes, e.g., Cu/Cu^{2+}, Zn/Zn^{2+}, can be used in TGCs, whereas there is a likelihood that the cyclicity and stability of TGCs are compromised due to irreversible corrosion. Considering reversibility, redox couples for TGCs are very limited, and there is marginal room to directly maneuver the reaction entropy. Nevertheless, tuning the local concentration of redox couples was demonstrated to be an effective strategy to improve thermoelectric properties remarkably.

Thermo-sensitive hydrogel as a local concentration regulator in TGCs

Regulating local concentrations of redox ions (C_{Red}/C_{Ox}) by using thermo-sensitive (or phase-transition) hydrogels is able to increase α [Figure 3B1], where C_{Red} and C_{Ox} is the concentration of ionic species at the oxidized state and reduced state, respectively. In 2016, Zhou *et al.* proposed the concept of thermo-sensitive supramolecular enhanced α of I^-/I_3^- in TGCs using α-Cyclodextrin (α-CD)[50]. The selective host-guest interaction of α-CD and I_3^- can capture redox-active I_3^- at a low temperature, thus increasing the C_{Red}/C_{Ox} and

Table 1. Typical redox couples in aqueous solution and their thermopower[43-49]

Redox reaction	Thermopower (mV K^{-1})	Type
$Fe(CN)_6^{3-} + e^- \leftrightarrow Fe(CN)_6^{4-}$	1.4	P
$Fe^{3+} + e^- \leftrightarrow Fe^{2+}$	-1.5 to -0.2	N
$I_3^- + 2e^- \leftrightarrow 3I^-$	-0.9 to -0.5	N
$V^{3+} + e^- \leftrightarrow V^{2+}$	-1.7	N
$Co(bpy)_3^{3+} + e^- \leftrightarrow Co(bpy)_3^{2+}$	-1.2	N

shifting the equilibrium toward the oxidation at the cold electrode, leading to an increased α from -0.86 to -1.4 mV K^{-1} and a power of 0.8 µW. Likewise, poly(N-isopropylacrylamide) (PNIPAM) hydrogel undergoes a coil-to-globule transition at a low critical solution temperature (LCST, ~32 °C)[51], which can work with a similar protocol and effectively tune α of I$^-$/I$_3^-$ redox couple[52]. Figure 5A and B show the mechanism of this thermo-sensitive pNIPAm hydrogel serving as a local concentration regulator, where the pNIPAm hydrogel captured I$_3^-$ at high temperature when it transformed from a hydrophilic state to a hydrophobic state, thus increasing the C_{Red}/C_{Ox} and shifting the equilibrium toward the oxidation at the hot electrode. Figure 5C gives the concentration change of I$^-$ and I$_3^-$ at different temperatures with and without the pNIPAm hydrogel, where the addition of pNIPAm hydrogel strongly decreased the concentration of redox-active I$_3^-$ while barely changed that of I$^-$. This concentration difference can be enlarged with increasing temperature and therefore leads to a reaction proceeding in the opposite direction compared with pristine I$^-$/I$_3^-$ redox couple, and an opposite open-circuit voltage (V_{oc}). In other words, the n-type nature of I$^-$/I$_3^-$ (α = -0.71 mV K^{-1}) was converted to p-type with the addition of pNIPAm hydrogel (α = 1.91 mV K^{-1}), and a power of 0.35 µW was achieved [Figure 5D and E]. Another candidate for thermo-sensitive hydrogel is methylcellulose (MC). Similar to pNIPAm, MC is a large molecule with hydrophobic methoxy groups, which switches from a hydrophilic state to a hydrophobic state at a temperature higher than 56 °C. The addition of MC into I$^-$/I$_3^-$ electrolytes [MC/(I$^-$/I$_3^-$)] captured I$_3^-$ and increased the C_{Red}/C_{Ox} at the hot electrode, resulting in a tunable α from -1.31 mV K^{-1} (T$_{cold}$ = 24 °C, T$_{hot}$ > 56 °C) to 1.48 mV K^{-1} (T$_{cold}$ = 24 °C, T$_{hot}$ < 56 °C) [Figure 5F and G][53]. Figure 5I shows the V_{oc} changed in response to the hot electrode temperature for TGCs containing different amounts of MC. The transition from n-type to p-type i-TE at around 56 °C could lead to the gelation of MC/(I$^-$/I$_3^-$). Besides, introducing small amounts of KCl substantially reduced the transition temperature to 32 °C and further boosted the α up to 9.62 mV K^{-1} in MC/(I$^-$/I$_3^-$)/KCl electrolytes [Figure 5J]. It was speculated that the binding between oxygen sites on MC and K$^+$ cations could facilitate the reversible complexation and dissociation of the K$^+$-MC-I$^-$/I$_3^-$ complex [Figure 5H and K], causing a larger entropy change for the I$^-$/I$_3^-$ redox couple. As a result, the maximum power of 0.12 and 0.36 mW m^{-2} K^{-2} were obtained for n-type and p-type TGCs, respectively [Figure 5L].

Hydrogel-enabled p-n TGC series
On the system level, the p-n series connection of TGCs (similar to traditional TE panels) is a straightforward approach to achieving pragmatically usable and large electric outputs and real wearable devices. However, traditional aqueous electrolytes restrict the large-scale integration and packing of TGC units[54]. As the quasi-solid electrolyte has been successfully applied to similar electrochemical energy systems, such as lithium-ion batteries[5,55], it reveals an alternative of polyelectrolyte for the p-n series connection of TGCs. Explicitly, hydrogel materials, e.g., poly(vinyl alcohol) (PVA)[39], polyurethane[52], cellulose[53,56], gelatin[18], and polyacrylamide (PAm)[57], have been tested as the quasi-solid matrix for series packing of TGCs. In 2016, Yang *et al.* reported a V_{oc} of ~0.7 V and a short-circuit current (I_{sc}) of 2 µA by utilizing body heat at an ambient temperature of 5 °C with the aid of 59 pairs of p-type PVA/(Fe(CN)$_6^{3-}$/ Fe(CN)$_6^{4-}$) and n-type PVA/(Fe^{2+}/Fe^{3+}) connected in a tandem structure [Figure 6A-E][39]. A similar design
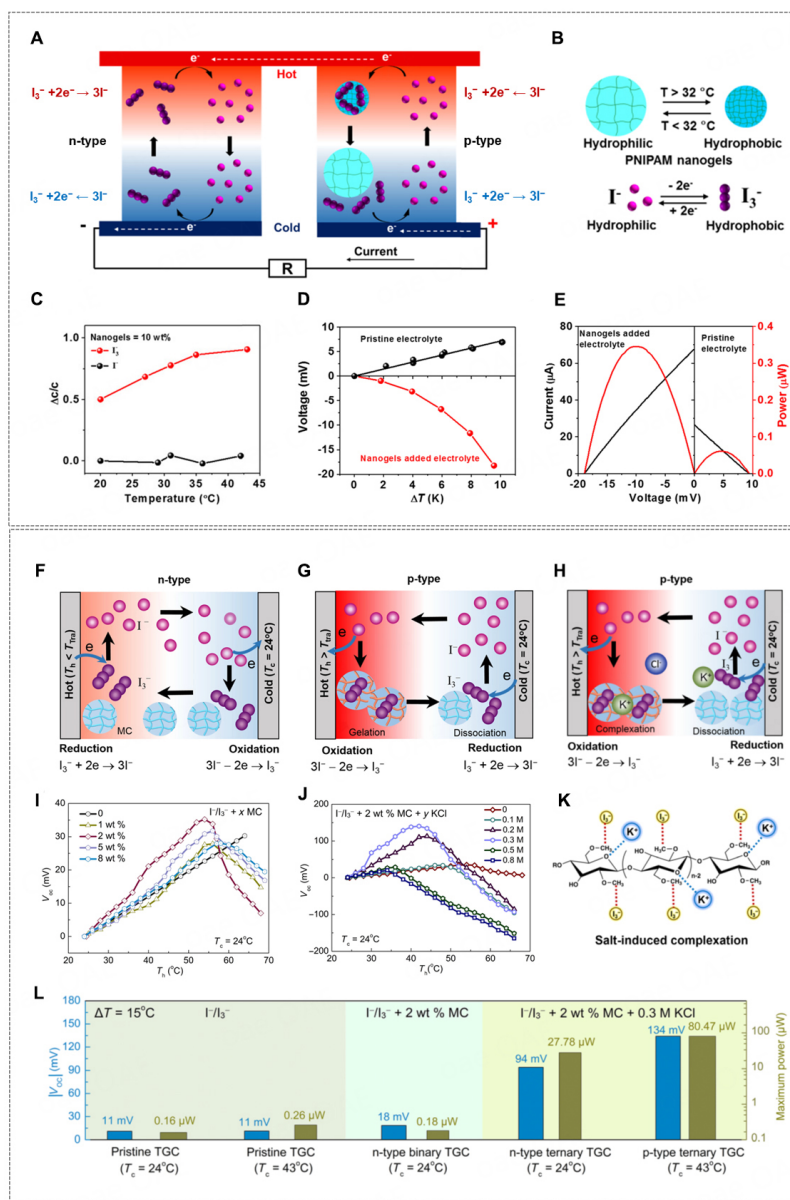
Figure 5. (A) Schematic of TGCs containing only I^-/I_3^- (n-type) and pNIPAm/(I^-/I_3^-) (p-type). (B) The phase change of pNIPAm nanogels and the redox reaction of I^-/I_3^-. (C) Concentration change ratio of I^- and I_3^- at different temperatures. (D) V_{oc} as a function of temperature difference with and without pNIPAm nanogels in the I^-/I_3^- electrolyte. (E) I-V curves and corresponding power at $\Delta T = 10$ K. (F and G) Schematic of TGCs containing MC/(I^-/I_3^-) at different temperatures, switching from n-type ($T_{hot} < T_{transition}$) to p-type ($T_{hot} > T_{transition}$). (H) Schematic of a TGC containing MC/(I^-/I_3^-)/KCl at $T_{hot} > T_{transition}$. (I) V_{oc} as a function of hot electrode temperature for various MC/(I^-/I_3^-) electrolytes with different MC amounts. The temperature of the cold electrode was 24 °C. (J) V_{oc} as a function of hot electrode temperature for 2 wt % MC/(I^-/I_3^-)/KCl with varying KCl amounts. The temperature of the cold electrode was 24 °C. (K) Salt-induced complexation, K^+ and I_3^- ions interacted with MC via O sites and methyl groups. (L) V_{oc} and maximum power for I^-/I_3^-, MC/(I^-/I_3^-), and MC/(I^-/I_3^-)/KCl TGCs. (A-D) Reprinted with permission from Ref.[52]. Copyright 2019 Elsevier. (E-K) Reprinted with permission from Ref.[53]. Copyright 2020 American Association for the Advancement of Science.

comprising 50 pairs of p-type polyurethane-pNIPAm /(I^-/I_3^-) and n-type polyurethane/(I^-/I_3^-) yielded a V_{oc} of ~1.0 V and a I_{sc} of 32 μA with body heat at an ambient temperature of 5 °C [Figure 6F-I][52]. Nevertheless, fully flexible TGCs were still limited by their substrates and encapsulation covers. The TGC fibers were then proposed[57,58]. Figure 6J illustrates a highly soft and stretchable TGC textile made of Pam/
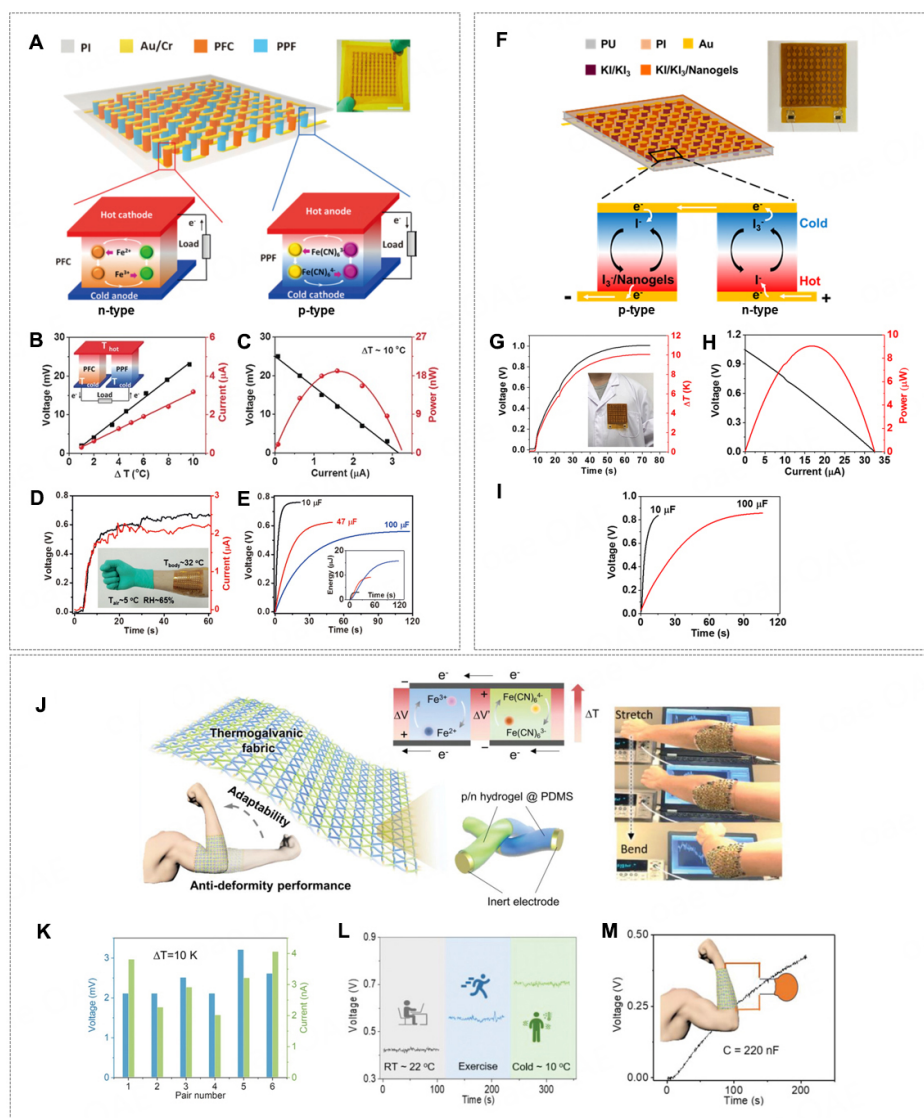
Figure 6. (A) 59 pairs of p-type PVA/(Fe(CN)$_6^{3-}$/Fe(CN)$_6^{4-}$) (PPF) and n-type PVA/(Fe^{2+}/Fe^{3+}) (PCF). The polyelectrolytes were sandwiched between two flexible substrates made of polyimide (PI). (B) V_{oc} as a function of ΔT. (C) *I-V* curve and the corresponding power density of one pair of p-n series. (D) V_{oc} and I_{sc} of 59 pairs of p-n series by using body heat at an ambient temperature of 5 °C. (E) V_{oc} of capacitors charged by 59 pairs of p-n series in (D). (F) Schematic and photo of 50 pairs of p-type polyurethane-pNIPAm /(I$^-$/I$_3^-$) and n-type polyurethane/(I$^-$/I$_3^-$). The nanogel in (F) stands for pNIPAm. (G) V_{oc} as a function of ΔT. (F) *I-V* curve and the corresponding power density of 50 pairs of p-n series by using body heat at an ambient temperature of 5 °C. (I) V_{oc} of capacitors charged by 50 pairs of p-n series in (G). (J) Soft and stretchable TGC textiles made of p-type Pam/(Fe(CN)$_6^{3-}$/Fe(CN)$_6^{4-}$) and n-type Pam/(Fe^{2+}/Fe^{3+}). (K) V_{oc} and I_{sc} at a ΔT = 10 K with different p-n pair numbers. (L) V_{oc} of the TGC textile worn on the arm in various scenarios. (M) V_{oc} of a 220 nF capacitor charged by the TGC textile worn on the arm at an ambient temperature of 10 °C. Reprinted with permission Ref.[39]. Copyright 2016, WILEY-VCH. (F-I) Reprinted with permission Ref.[52]. Copyright 2019, Elsevier. (J-M) Reprinted with permission Ref.[57]. Copyright 2021, WILEY-VCH.

(Fe(CN)$_6^{3-}$/Fe(CN)$_6^{4-}$, Fe^{2+}/Fe^{3+}) hydrogel fibers[57]. Polydimethylsiloxane (PDMS) served as an encapsulation coat for the hydrogels. Carbon nanotubes (CNTs) were added to PDMS to fabricate stretchable electrodes. As a whole, this all-soft TGC textile ensured close contact with the skin for body heat harvesting, generating V_{oc} up to ~0.7 V in a cold environment at 10 °C [Figure 6K-M].

Hydrogels in thermo-diffusion capacitors

The Soret effect that ions with opposite charges diffuse at different mobilities in response to a temperature gradient has been ignored because of its small contribution to the overall thermopower for most liquid-based i-TEs. It implies an opportunity to maximize the thermopower by manipulating ion mobilities in hydrogel materials, which can pose either chemical constraints like chelation or physical constraints such as coulombic attraction/repulsion to ionic species [Figure 3B]. In the last decade, a complementary i-TE (i.e., TDC) that capitalizes on distinct ion diffusions of anions and cations has attracted increasing attention. TDCs exhibit an up-to-date record of 43.8 mV K^{-1}, and the value is more than two orders higher than that of TEs[59]. Figure 4C shows the working mechanism of TDCs. Under a thermal gradient, the cations and anions with different mobilities (absolute values or directions) cause an electric field across the system. The thermopower of TDCs is $\alpha = -\frac{V(T_H)-V(T_L)}{T_H - T_L} = \alpha_{td}$, where α_{td} is the thermo-diffusion coefficient. Eastman entropy ($\hat{s}$) and standard single-ion heat of transport (Q^*) could be adopted to describe the ion transport of solvated ions under the thermal field, $\hat{s} = \frac{Q^*}{T}$. In the KCl solution where $n_+ = n_-$, the thermopower abides by $\alpha_{td} = \frac{(\hat{S}_+ D_+) - (\hat{S}_- D_-)}{e(D_+ + D_-)}$, where n and D are the numbers and the diffusion coefficient of ions, respectively[18]. However, neither $\hat{s}$ nor D could be obtained accurately in practice. Besides, other estimations, such as $\alpha_{td} = \frac{\hat{S}}{N_a |e|} = \frac{Q^*}{N_a |e| T}$, where N_a is the Avogadro number and $|e|$ is the charge of an electron, have been used to predict the theoretical thermopower yet lead to unsound results. For example, the thermopower of Na$^+$ cations was estimated to be 0.1 mV K^{-1} when the Q^* of 3 kJ mol^{-1} for Na$^+$ was applied. This thermopower is 100 times smaller than the empirical result of Na$^+$ (10 mV K^{-1}) in polyethylene glycol/sodium hydroxide (PEG/NaOH)[17,60]. As a matter of fact, it is extremely hard to apply the aforementioned estimation methods to liquid mixtures or hydrogels. Because there are numerous additional factors, including solvent transport, interactions of ionic species, solute concentration, pressure, *etc.*, which all behave according to less understood mechanisms[60-65]. In short, large thermopowers observed in recent works relying on thermo-diffusion still lack rigorous explanation, and other possible mechanisms, such as temperature-dependent dissociation/binding of ions and other thermal effects of electrolyte-electrode interfaces, also need to be taken into account[66].

Hydrogel as ion dissociable polyelectrolyte in TDCs

Hydrogel is ideal as a polyelectrolyte because it provides dissociable ions and a low-viscous background for mass and ion transport and offers sufficient and versatile pendant groups for regulating ion behaviors [Figure 3B2]. A typical example is a poly(sodium 4-styrenesulfonate) (PSSNa) hydrogel, where Na$^+$ cations are diffused against the fixed negatively charged PSS$^-$ backbones at a thermal gradient, exhibiting an α of 4 mV K^{-1}[67]. Because ions cannot pass across the electrolyte-electrode interface to the external circuit as electrons or holes can, TDCs deliver intermittent discharging current that decreases over time to zero when TDCs are connected to external loads. In 2016, a 4-stage charging-discharging cycle of TDC and its theoretical model were proposed by Zhao and Wang *et al.* and a large thermopower was attained with the controlled ion transport in NaOH-treated polyethylene glycol (NaOH-PEO)[17,67]. The hydroxyl groups (-C-OH) on the PEO were transformed into anionic alkoxide end-groups (-C-O-Na), resulting in polymeric anions with low mobility but Na$^+$ cations with high mobility. Figure 7A and B show the capacitor-like 4-stage charging-discharging cycle of the TDC comprised of Au/CNT electrodes and NaOH-PEO electrolyte, (i) V_{oc} increased while a ΔT of 16 K was applied, corresponding to the Na$^+$ cations diffusing to the cold electrode; (ii) R_{load} (100 kΩ) was connected, and V_{load} decreased while the charges were transferred to the CNT-Au electrodes; (iii) The circuit was disconnected, and ΔT was removed. V_{oc} further decreased while the ions moved back along with the re-distribution of cations and anions. The remaining charges on the electrodes are responsible for the observed V_{oc} with a reversed voltage direction (compared with V_{oc} in
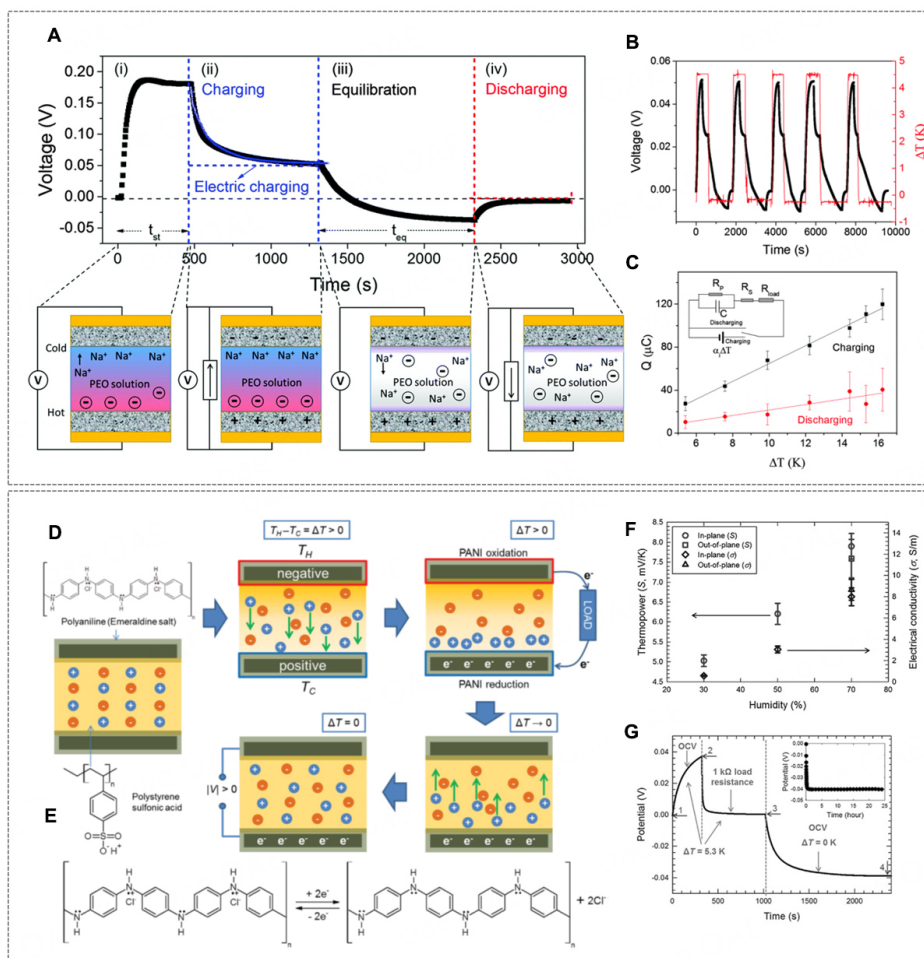
Figure 7. (A) Schematic of 4-stage charging-discharging cycle of TDC made of NaOH-PEO electrolyte and Au/CNT electrodes at a ΔT = 16 K (R_{load} = 100 kΩ). (B) V_{oc} of NaO-[CH2-CH2-O]$_n$-Na TDC during charging and discharging by applying a periodic heating source. (C) The charges being transferred during charging (black squares) and discharging (red circles) at different ΔT (R_{load} = 100 kΩ). (D) Schematic of a TDC made of PSSH polyelectrolyte and PANI electrodes. (E) Redox reactions of PANI during charging and discharging processes (switching between emeraldine salt and leucoemeraldine base). (F) α and electrical conductivity of PSSH TDC at various humidities and measured at different configurations, i.e., in-plane and out-of-plane. (G) 3-stage charging-discharging cycle of PSSH TDC at a ΔT = 5.3 K (R_{load} = 1 kΩ). (A-C) Reprinted with permission Ref.[17]. Copyright 2016, The Royal Society of Chemistry. (D-G) Reprinted with permission Ref.[68]. Copyright 2016, WILEY-VCH.

stage I); and (iv) the TDC was discharged and provided useful energy to the external load. Accordingly, the charges being transferred to the electrodes at stage (ii) ($Q_{charging}$) is highly related to the capacity of electrodes, eventually affecting the overall energy efficiency. In particular, the Au/CNT (1031 µF cm^{-2}) outperformed bare Au electrodes (5.1 µF cm^{-2}) for a $Q_{charging}$ = 2.42 × 10^{-5} C [Figure 7C] and a peak energy efficiency of 5 × 10^{-4}% at a ΔT = 4.5 K, while the Au electrodes lost its voltage immediately because of the small capacitance.

Besides inert electrodes (e.g., carbon, gold, and platinum), redox-active electrodes, such as polyaniline (PANI) conducting polymers, were incorporated to transduce the gradient energy of ions in the polyelectrolyte to the PANI electrode via electrochemical reactions. Particularly, the PANI were thermally charged to an oxidation state (leucoemeraldine base at high temperatures) or reduction state (emeraldine salt at low temperatures) [Figure 7D and E]. Additionally, the PANI deposited on highly porous flower-
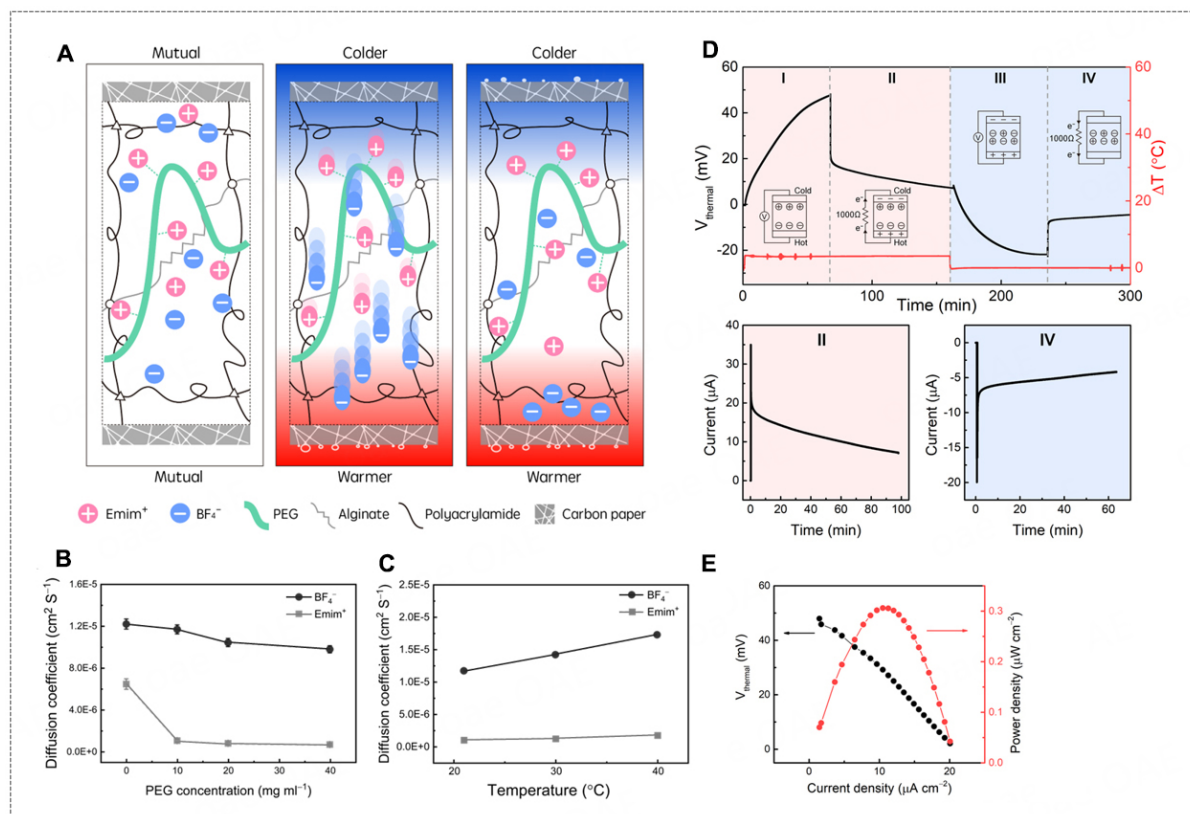
Figure 8. (A) Schematic of Pam-alginate/EmimBF$_4$/PEG TDC. (B) Diffusion coefficients of Emim$^+$ and BF$_4^-$ as a function of PEG concentration. (C) Diffusion coefficients of Emim$^+$ and BF$_4^-$ as a function of temperature. (D) 4-stage charging-discharging cycle of Pam-alginate/EmimBF$_4$/PEG TDC at a ΔT = 3.4 K (R_{load} = 1 kΩ). (E) *I-V* curve and the corresponding power density of Pam-alginate/EmimBF$_4$/PEG TDC at a ΔT = 3.1 K. Reprinted with permission Ref.[8]. Copyright 2021, Elsevier.

shaped graphene structures entangled by tubular CNTs (1200 F m^{-2}) were assembled with poly(4-styrenesulfonic acid) (PSSH) polyelectrolytes, where an α of 8 mV K^{-1} at a relative humidity (RH) of 70% was obtained [Figure 7F][68]. Compared with inert electrodes, these redox-active electrodes held the voltage even after the temperature gradient was removed [Figure 7G]. Moreover, it is worth noting that the RH greatly shifted the measured thermopower from 5 mV K^{-1} (RH = 30%) to 8 mV K^{-1} (RH = 70%) when the sample was tested with in-plane configuration, implying an underlying water transport related mechanism when a large surface area of hydrogel polyelectrolyte was exposed to the ambient air[69,70].

Hydrogel as an intermediate to regulate ion transport in TDCs
Aside from directly dissolving ions from polymer backbones, a hydrogel can also serve as a medium to house ionic species (i.e., cations and anions), inside which other polymer additives can modify the mobilities of cations and anions to generate very high thermopowers [Figure 3B3]. As an example, the double-network PAm-alginate hydrogel was carefully selected first for its water content of about 86%, which allows the ionic liquid of EmimBF$_4$ to be used as the electrolyte and be dissociated sufficiently; second, the alginate endowed with substantial carboxyl functional groups can localize Emim$^+$ ions; third, the PEG was added to further impede the ion transport of Emim$^+$ through hydrogen bonding [Figure 8A][8]. As a result, a large disparity of the mobility between Emim$^+$ and BF$_4^-$ was created, and therefore a very high thermal voltage was obtained when a temperature gradient was built, corresponding to an α of 19.32 mV K^{-1}. The distinct mobilities of cations and anions [Figure 8B and C] at different temperatures were, for the first time,
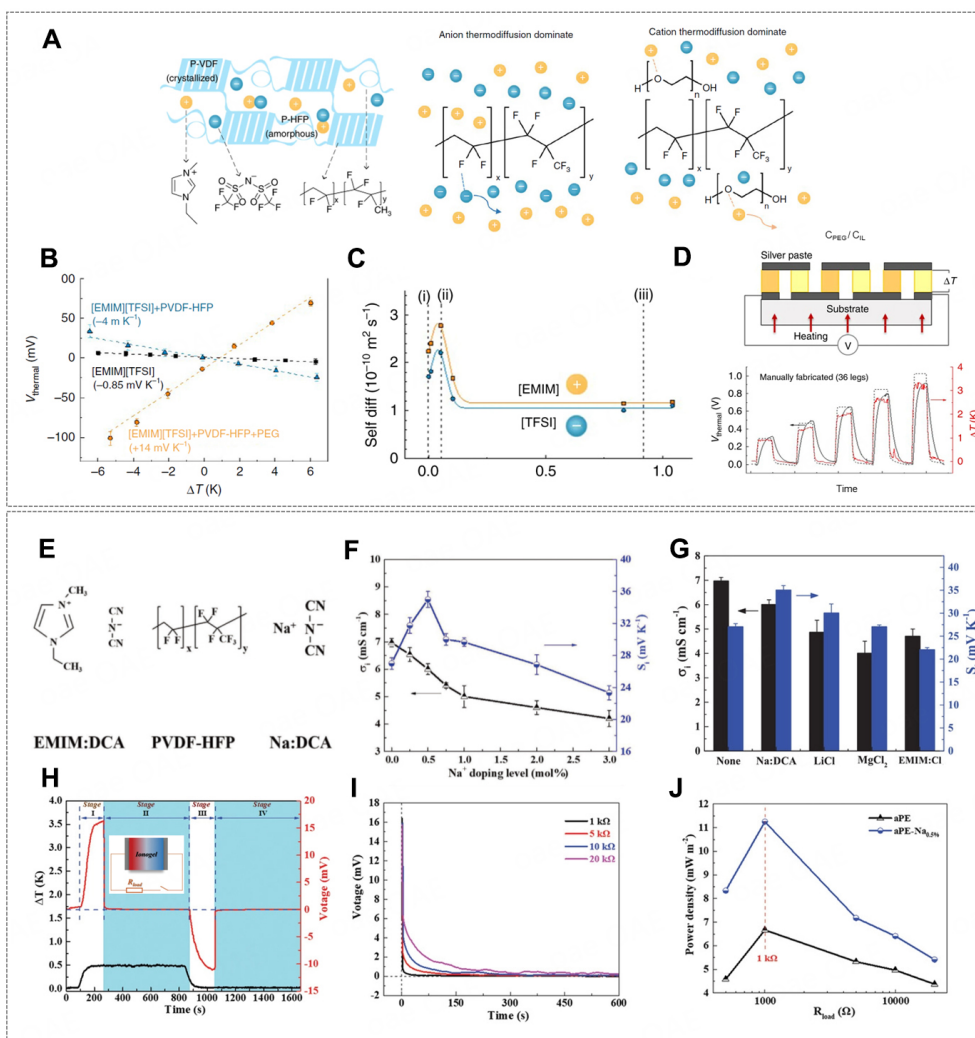
Figure 9. (A) Schematic of PVDF-HFP/EmimTFSI TDC, with and without PEG addition. (B) V_{oc} of EmimTFSI, PVDF-HFP/EmimTFSI, and PVDF-HFP/EmimTFSI/PEG as a function of ΔT. (C) Diffusion coefficient of $Emim^+$ and $TFSI^-$ with different PEG content. (D) V_{oc} of 18 pairs p-type PVDF-HFP/EmimTFSI/PEG and n-type PVDF-HFP/EmimTFSI connected in series at different ΔT. (E) Chemical structures of EmimDCA, PVDF-HFP, and NaDCA. (F) Ionic conductivity and α of PVDF-HFP/EmimDCA/NaDCA TDC as a function of Na^+ doping. (G) Ionic conductivity and α of PVDF-HFP/EmimDCA with different dopants at the concentration of 0.5 mol% with respect to EmimDCA. (H) The 4-stage charging-discharge cycle of PVDF-HFP/EmimDCA/NaDCA at a $\Delta T = 0.5$ K ($R_{load} = 5$ kΩ). (I) Voltage during stage II with different R_{load}. (J) Average power density as a function of R_{load} with and without NaDCA. (A-D) Reprinted with permission Ref.[71]. Copyright 2019, The Author(s), Nature publishing group. (E-J) Reprinted with permission Ref.[59]. Copyright 2022, Wiley-VCH.

characterized by 2D-diffusion-ordered spectroscopy (DOSY) nuclear magnetic resonance (NMR), allowing a quantitative analysis of ion transport inside the hydrogel (or polyelectrolyte) rather than intuitive assumptions. The voltage profile during charging-discharging of a PAm-alginate/EmimBF₄/PEG is shown in Figure 8D and E, and a maximum power density of 0.31 μW cm⁻² was achieved at a ΔT of 3.1 K. Another example of using polymer additives to regulate ion transport is PEG in poly(vinylidene fluoride-co-hexa-fluoropropylene) (PVDF-HFP) with EmimTFSI ionic liquid [Figure 9A][71]. In pristine PVDF-HFP/EmimTFSI gel, fluorine atoms on the polymer matrix serving as the strong electron-withdrawing groups were likely to increase the local molecular order and enhance the thermo-diffusion of anions, contributing to the α of -4 mV K⁻¹ for PVDF-HFP/EmimTFSI. After adding PEG into PVDF-HFP/EmimTFSI gel, the oxygen atoms in the PEG molecules were likely to enhance the thermo-diffusion of cations over anions,

thus tuning the α from -4 to 14 mV K^{-1} [Figure 9B and C]. In addition, a PVDF-HFP/EmimDCA/NaDCA TDC was reported to reach a large α from 25.5 to 43.8 mV K^{-1} by using 0.5 mol% sodium dicyanamide (NaDCA) additive to EmimDCA [Figure 9E-G][59]. An increased mobility difference between cations and anions originates from Na$^+$ cation doping. The p-type nature of PVDF-HFP/EmimDCA indicates DCA$^-$ moves slower than Emim$^+$ in the gel matrix, corresponding to an α of 25.5 mV K^{-1}. After adding NaDCA, the relatively strong Coulomb attraction between Na$^+$ and DCA$^-$ ions hindered the diffusion of DCA$^-$ ions, thus enlarging the mobility difference. In contrast, Cl$^-$ anion doping (adding EmimCl) had the opposite effect, which hindered the diffusion of Emim$^+$ and decreased the α from 25.5 to 22.0 mV K^{-1}. Moreover, other dopants like lithium chloride (LiCl) and magnesium chloride (MgCl$_2$) barely changed α as they slowed down both cations and anions in the gel matrix, where no further mobility difference between cations and anions could be developed [Figure 9G]. As a result, PVDF-HFP/EmimDCA/NaDCA outperformed other systems and exhibited a maximum power density of 11.2 mW m^{-2} with a R_{load} of 1 kΩ at a ΔT of 0.5 K [Figure 9H-J]. It is worthwhile noting that the solid-state NaDCA has a higher lattice energy, where Na$^+$ is speculated to form strong bonding with DCA$^-$ to prevent DCA$^-$ from moving. In other words, melting point might be used as an indicator to predict the effect of dopants on the ion mobility of ionic liquids.

Hydrogel as an ion channel in TDCs
Instead of regulating ion transport inside a homogeneous medium, the hydrogel can be fabricated with a physical channel structure, further improving the capability to localize ions or promote ion transport [Figure 3B4]. Kim *et al.* designed a Cl$^-$ channel by using poly(3,4-ethylenedioxythiophene) polystyrene sulfonate (PEDOT:PSS) hydrogel containing cupric chloride (CuCl$_2$) as a functional additive[72]; there was strong metal binding between Cu^{2+} and PSS polymer chains [Figure 10A]. In the PEDOT:PSS dispersion, the hydrophilic PSS polyanion shell prevented the agglomeration of PEDOT:PSS clusters [Figure 10B]. After adding CuCl$_2$, the strong ionic cross-linking of Cu^{2+} and PSS shells pulled the clusters together and left a free water/anion channel in the wet conductive gel, which can be seen from the time-of-flight secondary ion mass spectrometry (ToF-SIMS) map of the Cl$^-$ distribution image [Figure 10C]. This channel permitted the ion transport of Cl$^-$ under the temperature gradient, therefore the p-type nature of the pristine PEDOT:PSS was converted to n-type with a negative thermopower of -18.2 mV K^{-1}. A fluorescence image showing the color change in response to local Cl$^-$ concentration indicated Cl$^-$ transport at the temperature gradient [Figure 10D and E]. In contrast to the Cl$^-$ channel, Figure 10F and G illustrate a design using an asymmetric PVA channel to selectively localize Cl$^-$ anions but transport H$^+$ cations[73]. This H$^+$ channel was manufactured by orientated tensile crystallization of physically cross-linked PVA hydrogel. More specifically, PVA hydrogel was made to be less crystallized on the hot side, but it was highly crystallized on the cold side. When hydrated H$^+$ cations and Cl$^-$ anions were driven by the temperature gradient from the amorphous region to the crystalized region, these ions firstly experienced dehydration, then the H$^+$ cations with a small radius could reach the cold side, whereas Cl$^-$ anions were blocked by the highly crystalized PVA. As a result, an α of 38.2 mV K^{-1} was achieved [Figure 10H-J][73].

Hydrogel-enabled p-n TDC series
Hydrogel-based TDCs can be connected and packed to form p-n series to enhance voltage output[71,73]. P-n pairs of PVDF-HFP/PEG/EmimTFSI with an α of 14 and -4 mV K^{-1} can be either manually assembled or screen-printed [Figure 9D][71]. 18 p-n pairs generated about 1 V at ΔT = 3 K, corresponding to 94% of the sum of individual thermoelectric legs. Whereas 20 p-n pairs made by screen-printing only exhibited the α of 182 mV K^{-1}, which probably resulted from electrodes being short-circuited.

Synergistic effect of thermo-diffusion and redox reaction
Generally, TGCs with thermogalvanic effect provide small thermal voltage but large current, while TDCs with thermo-diffusion effect provide large thermal voltage but small current. To pursue i-TEs with high
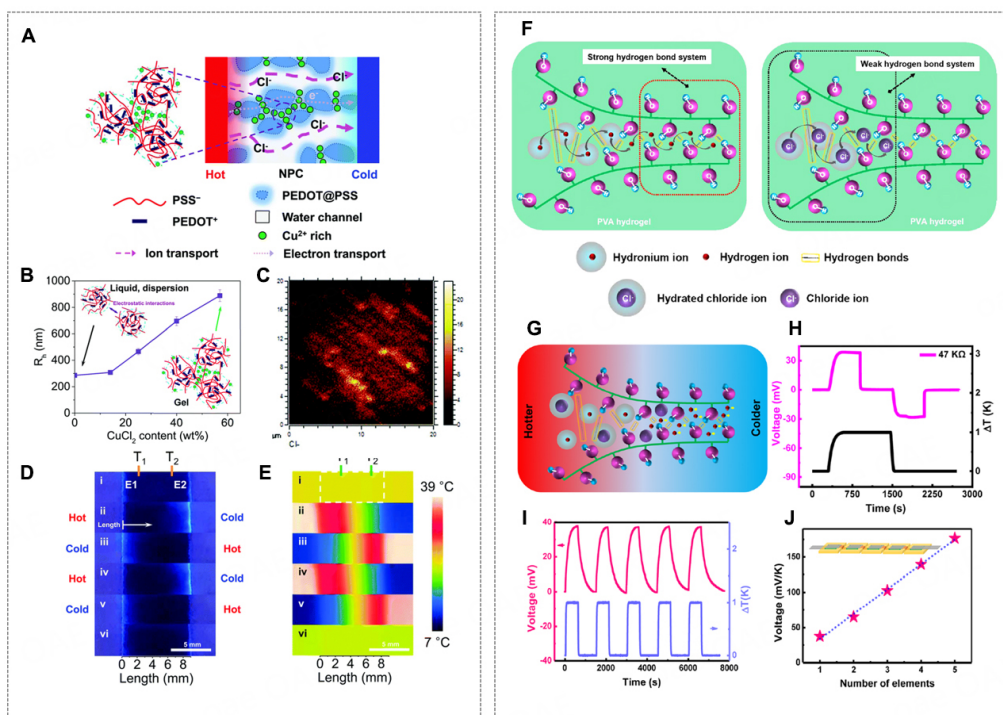
Figure 10. (A) Schematic of PEDOT:PSS/CuCl$_2$ TDC. (B) Hydrodynamic radius (R_h) of PEDOT:PSS/CuCl$_2$ particles in the diluted solutions. (C) ToF-SIMS map of the Cl$^-$ distribution on the cross-section. (D) Cl$^-$ fluorescence mapping in heating-cooling cycles of the PEDOT:PSS/CuCl$_2$ TDC under UV lamp and (E) corresponding thermal images. (F) Schematic of PVA/HCl TDCs and H$^+$ channels. (G) Schematic illustration of ions in PVA/HCl TDC at a ΔT. (H) 4-stage charging-discharging cycle of PVA/HCl TDC at a $\Delta T = 1$ K ($R_{load} = 47$ kΩ). (I) V_{oc} in response to periodic heating. (J) V_{oc} of PVA/HCl TDCs connected in series at a $\Delta T = 1$K. (A-E) Reprinted with permission Ref.[72]. Copyright 2020, The Author(s), The Royal Society of Chemistry. (F-J) Reprinted with permission Ref.[73]. Copyright 2016, WILEY-VCH.

energy conversion efficiency in terms of both voltage and current, the integration of two systems in one hydrogel-based i-TE was proposed. In a rationally designed i-TE comprising p-type and n-type elements, there is a chance for the effects, i.e., thermogalvanic effect of redox couple and Soret effect of salt ions, to promote but not to cancel each other [Figure 11A-C]. Starting the hypothesis that thermopowers can be added or subtracted, the i-TE hybrid using gelatin that combined the thermogalvanic effect of Fe(CN)$_6^{4-}$/Fe(CN)$_6^{3-}$ ($\alpha_r < 0$, i.e., $\alpha > 0$) and the Soret effect of KCl ($\alpha_{td} > 0$, i.e., $\alpha > 0$) was reported by Han *et al.*, where TGC and TDC elements mutually reinforced faradic redox reactions and asymmetric ion transport of K$^+$ over Cl$^-$ [Figure 11D][18]. A positive thermopower of 17.0 mV K^{-1} was obtained, and the estimated contribution from each effect is shown in Figure 11E, as 10.2% from gelatin hydrogel (thermo-diffusion of H$^+$ from the ionization of -COOH group), 17.9% from Fe(CN)$_6^{3-}$/Fe(CN)$_6^{4-}$ redox entropy change, 9.7% from thermo-diffusion of K$_3$Fe(CN)$_6$ and K$_4$Fe(CN)$_6$, and 62.2% from thermo-diffusion of KCl. To date, gelatin/(Fe(CN)$_6^{3-}$/Fe(CN)$_6^{4-}$)/KCl gave the recorded high power density of 0.66 mW m^{-2} K^{-2} for one single i-TE. Figure 11F and G show the quasi-continuous charging-discharging process of the system, where the cell was discharged for 10 s and recharged for 3 mins at a ΔT of 8.5 K for 100 cycles. A maximum power density of 0.66 mW m^{-2} K^{-2} was achieved. Furthermore, when connected to a R_{load} of 5,000 Ω, the cell reached a relatively steady stage with the highest energy density of 12.8 J m^{-2} [Figure 11H and I]. Finally, a V_{oc} of 2 V and peak power of 5 μW were achieved using body heat by connecting 25 unipolar i-TEs at a ΔT of 10 K [Figure 11J and K]. From a device perspective, this high electric output would be able to power small electronics like IoT sensors (pressure or temperature sensors, accelerometers, *etc.*) without using amplifiers[74].
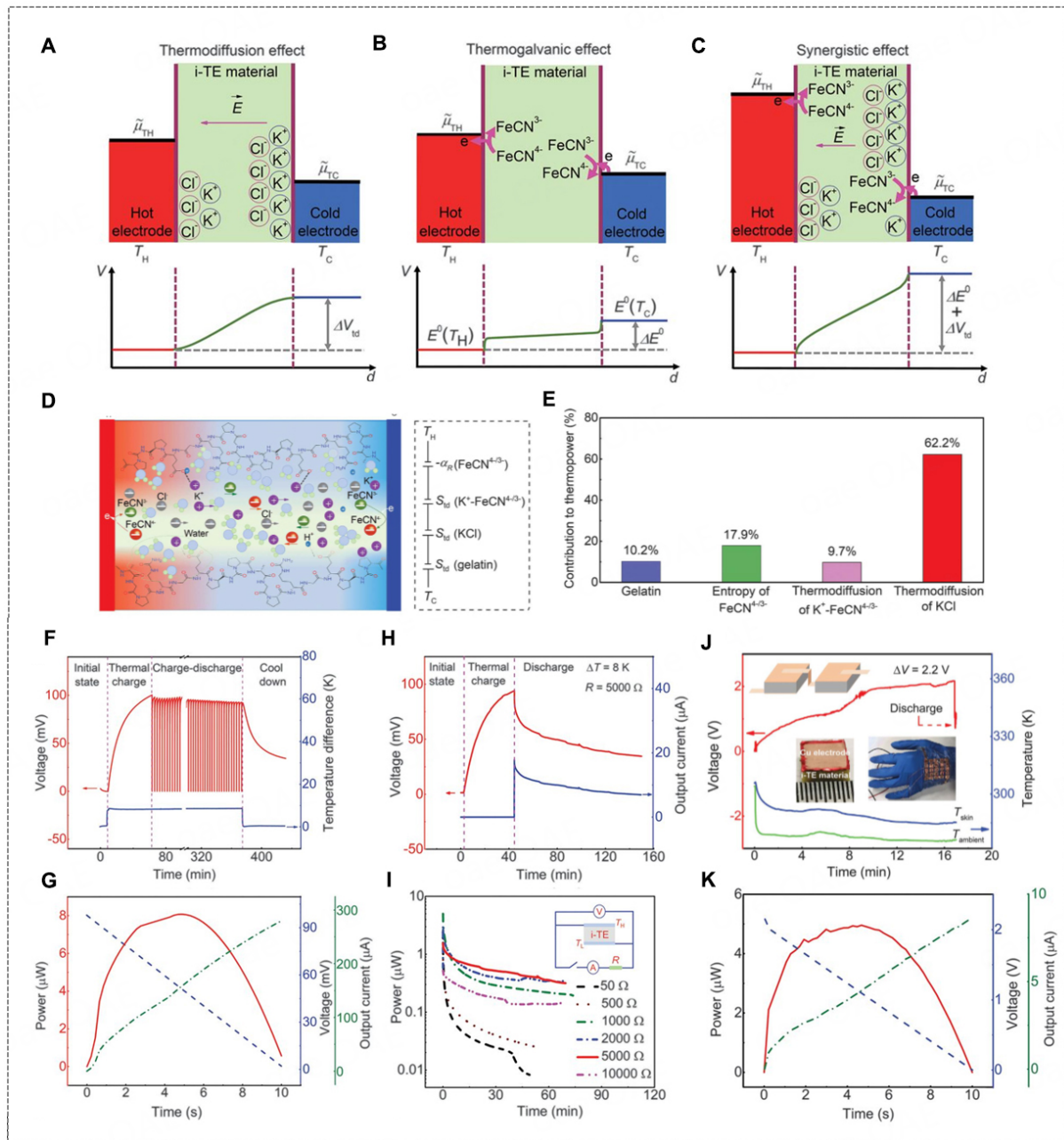
Figure 11. Schematic potential profile of (A) gelatin/KCl, (B) gelatin/($Fe(CN)_6^{3-}$/$Fe(CN)_6^{4-}$), and (C) gelatin/($Fe(CN)_6^{3-}$/$Fe(CN)_6^{4-}$)/KCl i-TEs. (D) Schematic illustration of diffusion, redox reactions, and interaction of various ions in gelatin/($Fe(CN)_6^{3-}$/$Fe(CN)_6^{4-}$)/KCl i-TE at a ΔT. (E) The fractional contribution of each effect to α in gelatin/($Fe(CN)_6^{3-}$/$Fe(CN)_6^{4-}$)/KCl i-TE. (F) V_{oc} of the i-TE in quasi-continuous charging-discharging at a ΔT = 8.5 K for 100 cycles. (G) Power, voltage, and current during the fifth discharging in (F). (H) Voltage and current during discharging at a ΔT = 8 K with R_{load} = 5 kΩ. (I) Power as a function of discharging time using different R_{load}. (J) V_{oc} of 25 i-TEs connected in series worn on hand at a ΔT = 10 K. (K) Power, voltage, and current of the device in (J). Reprinted with permission Ref.[18]. Copyright 2020, The American Association for the Advancement of Science.

Challenges for hydrogel-based i-TEs

Table 2 summarizes most of the best i-TEs, in which (poly)electrolytes, electrodes, test conditions, thermopower, and power output are documented for a comprehensive comparison. Efforts to improve electric outputs at a low-grade heat range have given many gratifying results over the past decade using

Table 2. Some of best reported i-TEs

Ref*	Type	Material (Polymer/(redox couples)/other)	Electrode	Test configuration	ΔT (K)	α (mV K^{-1})	Power** (mW m^{-2} K^{-2})	Energy efficiency (%)
TGC TDC hybrid[18]	p	Gelatin	Cu, Cu/Au	Out-of-plane	8.5	1.3		
	p	Gelatin/($Fe(CN)_6^{3-}$/$Fe(CN)_6^{4-}$)				4.8		
	p	Gelatin/KCl				6.7		
	p	Gelatin/($Fe(CN)_6^{3-}$/$Fe(CN)_6^{4-}$)/KCl				17	0.66	
TGC[39]	n	PVA/(Fe^{3+}/Fe^{2+})	Au/Cr	Out-of-plane	17.5	-1.02	0.0236 (ΔT = 20 K)	
	p	PVA/($Fe(CN)_6^{3-}$/$Fe(CN)_6^{4-}$)				1.21		
TGC[70]	p	PAm/($Fe(CN)_6^{3-}$/$Fe(CN)_6^{4-}$)/K$^+$, Li$^+$, Br$^-$	Ti	Out-of-plane	16	1.2	0.007 (ΔT = 20 K)	
TGC[56]	n	Cellulose/($Fe(CN)_6^{3-}$/$Fe(CN)_6^{4-}$)	Ni	Out-of-plane	15	-1.38	0.0622	
TGC[41]	p	AM-co-AMPS/($Fe(CN)_6^{3-}$/$Fe(CN)_6^{4-}$)/NaCl	Pt	In-plane	13	1.6	0.61 (ΔT = 40 K)	0.16
TGC[50]	n	(I^-/I^{3-})	Pt wire	/	34	-0.86		1 × 10^{-4}
	n	α-CD/(I^-/I^{3-})				-1.45	0.00129	3 × 10^{-4}
	n	α-CD/(I^-/I^{3-})/KCl				-1.97	0.0147	3 × 10^{-3}
TGC[52]	n	(I^-/I^{3-})	Graphite	Out-of-plane	10	-0.71	0.05 (µW)	
	p	pNIPAm/(I^-/I^{3-})				1.91	0.35 (µW)	
TGC[53]	n	(I^-/I^{3-})	Graphite	Out-of-plane	/	-0.71	0.16 (µW) (ΔT = 15 K)	
	n, p	MC/(I^-/I^{3-})				-1.32 to 1.48	(n-type) 0.18 (µW) (ΔT = 15 K)	
	n, p	MC/(I^-/I^{3-})/KCl				-8.18 to 9.62	(n-type) 0.12 (p-type) 0.36 (ΔT = 15 K)	
TDC[17]	p	NaOH-PEO	Au/CNT	Out-of-plane	5	11.1		5 × 10^{-4}
TDC[68]	p	PSSH	PANI/CNT	Out-of-plane, In-plane	5	8		
TDC[67]	p	PSSNa	Au	In-plane	4	4		0.004
TDC[71]	n	EmimTFSI	Ag, NFC/CNT, Ti/Au	In-plane	6	-0.85		
	n	PVDF-HFP/EmimTFSI				-4		
	n, p	PVDF-HFP/EmimTFSI/PEG				-4 to 14		
TDC[7]	p	TEMPO-oxidized cellulose membrane/NaOH-PEO	Pt	Out-of-plane	20	24		

Ref	Type	Material	Electrodes	Configuration				
TDC[72]	p	PEDOT:PSS	Au, CNT/Au	In-plane	4	7.5		
	n	PEDOT:PSS/CuCl$_2$				-18.2	0.0188 (ΔT = 4.5 K)	0.34
TDC[8]	p	PAm-Alginate/LiBF$_4$	Carbon paper	Out-of-plane	8	1.85		
	p	PAm-Alginate/EmimBF$_4$				5.61		
	p	PAm-Alginate/EmimBF$_4$/PEG				19.32	0.326 (ΔT = 3.1 K)	
TDC[66]	p	Nafion	Carbon paint	In-plane	5	4.2		
	p	S-PEEK				5.5		
	n	PVA/NaOH				-1		
	p	PVA/H$_3$PO$_4$				1.6		
	p	PDDAC				19		
TDC[75]	p	PVDF-HFP/EmimDCA	Ag, Au, Cu	In-plane	0.5	26.1	0.00233 (ΔT = 0.6 K)	
	p	PVDF-HFP/EmimTFSI				2		
	p	PVDF-HFP/BmimBF$_4$				6		
	p	Agarose/EmimDCA				11.9		
	p	PVA/EmimDCA				13.5		
	p	Gelatin/EmimDCA				22.1		
	p	PVDF/EmimDCA				23.1		
TDC[40]	p	Polyurethane/EmimDCA	Ag	In-plane	0.7	34.5		
TDC[59]	p	PVDF-HFP/EmimDCA	Ag	In-plane	0.35	29	26.8 (ΔT = 0.5 K)	
	p	PVDF-HFP/EmimDCA/NaDCA				43.8	44.8 (ΔT = 0.5 K)	
TDC[73]	p	PVA/HCl	Carbon	Out-of-plane	1	38.20		
	p	PVA/HNO$_3$				18.50		
	p	PVA/H$_2$SO$_4$				12.26		

*Values correspond to the state-of-art results denoted in the references; **ΔT for the measurement of power output that is different from thermopower measurement is indicated.

hydrogels and their analogs. Attention is now moving to the next stage of real device power, which is still low compared with other miniaturized energy conversion counterparts. Also, the inconsistency in experimental measurements and calculation methods create obstacles to future developments. Concerning experiments, the temperature gradients are very different in terms of value and direction (in-plane and out-of-plane) in various cases. Some very high thermopower outputs were reported with extremely small temperature gradients (≤ 1 K) or were measured at in-plane configurations[40,59,73]. Unfortunately, the

inaccuracy of thermopower characterization became obvious when decreasing the temperature difference, as the systematic error may dominate the results. A proper way is to assess the thermopower at both small and moderate temperature differences (e.g., from 1-50 °C). Meanwhile, in-plane measurements in an open environment (without strict encapsulation) could lead to misinterpretation of electric responses because the effect of the solvent may be more pronounced than that of solutes, which is likely to cause the hydrovoltaic phenomena (this will be discussed in the next session). Thus, a reliable encapsulation is essential for accurate measurement of the thermopower as well as preventing water loss for maintaining long-term cyclability. Several encapsulating methods, such as soft substrate sealing[39,52], (vacuum) heat-sealing[8,18], hydrophobic elastomer coating[57], *etc.*, have been applied to hydrogel-based i-TEs so far. Besides, the electrode materials (i.e., inert electrodes of gold, carbon, *etc.*, and redox-active electrodes of Cu, PANI, *etc.*) primarily dictate the working mechanisms, which should be carefully used and studied[18]. Intrinsic thermoelectric responses stemming from designated redox reactions or latent corrosion of electrode materials should be taken into account when evaluating the overall thermopower of the device, where the latter is detrimental to the long-term stability and reversibility. In short, the measurement conditions need to be clearly stated, and multi-temperature gradients with accurate ΔT are essential for assessing thermopower. Secondly, since TGCs and TDCs abide by different technical origins and both are deviated from solid TEs, a valid and predictable model is required to improve accuracy for the evaluation of a "new" figure of merit, power density, and energy conversion efficiency. So far, the performance of i-TEs has been calculated by various means, so they cannot be fairly compared from work to work. Thirdly, the absence of comprehensive theory hinders the understanding of hydrogel-based i-TEs and further exploits i-TE designs. With increasing ion concertation and the involvement of soft, charged, and confined interfaces (of hydrogel polymer) in i-TE systems, Debye length, ion solvation, and even the local dielectric constant are hard to be predicted using conventional models. There is a lack of awareness of microcosmic interactions among water, hydrogel polymers, and ionic species, especially in non-equilibrium thermal fields and among water-polymer binary systems. The interpretation of thermo-electrochemical phenomena in such systems without *in-situ* quantitative evidence is equivocal. Particularly for TDCs, although it is generally believed that the distinct ion mobilities of anions and cations and the consequent asymmetric charge distribution on a temperature gradient are the causes of thermopower, little experimental evidence was provided to show the differences in ion mobilities[8], while some other observations indicated this explanation was insufficient[67]. In conclusion, a careful investigation into the mechanism of the hydrogel-based i-TEs is very much needed in the future.

HYDROVOLTAIC TECHNOLOGIES USING HYDROGEL MATERIALS

Water empowers the biggest energy reservoir on the Earth as it absorbs the tremendous energy of 115 W m^{-2} from solar radiation[76,77]. The energy carried by water emerges in various forms, such as ambient moisture, water droplets, water vapor, *etc*. [Figure 12A]. Hydrovoltaic technology refers to the production of electricity from direct interactions between water molecules and functional materials[78], which fundamentally shares the similar mechanism of TDCs that is dictated by ion transport. Like the behaviors in TDCs, the gradient energy of water can be converted into the asymmetric distribution of charge carriers and simultaneously produce electric signals. Since Huang *et al.*, Cheng *et al.*, and Huang *et al.* have pioneered the work of graphene-based moisture-enabled generators (MEGs)[79-81], graphene strips with sliding ionic solution (or droplets)[82-85], and water evaporation-driven nanogenerators[86,87], the following research in recent years has yielded a variety of auspicious hydrovoltaic devices [Figure 12B]. The confidence of energy transduction from water to electricity has been strengthened, and there is a growing trend of using hydrogel materials for hydrovoltaic devices.
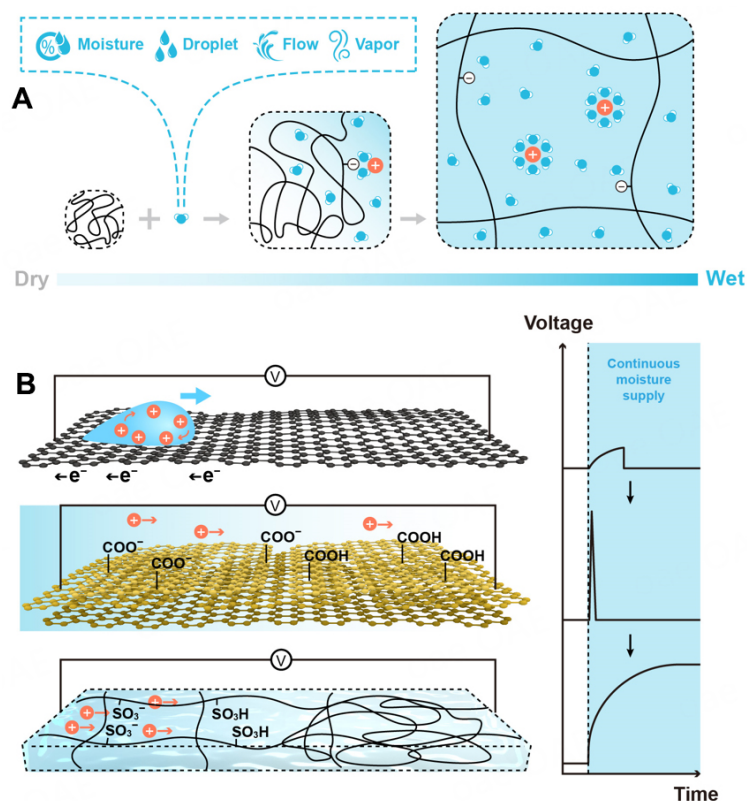
Figure 12. (A) Some common water sources can be harnessed with hydrovoltaic media and a schematic illustration of ions dissociation from the hydrogel backbones after imbibing moisture. (B) Three types of hydrovoltaic media and corresponding characteristic electric outputs, top: graphene with moving droplet of ionic solution; middle: graphene oxide; bottom: polyelectrolyte hydrogel.

A number of previous studies have postulated convergence criteria pertaining to ideal media for transduction of a water gradient to electricity, including fast water absorption/desorption kinetics, high density of polar functional groups (or high zeta-potential), large surface area of the materials, and high-speed mass transport. Hydrogel materials answer these demands properly as their 3D network of hydrophilic polymers is endowed with desirable water absorption and retention properties and fast mass and ion transport features. Besides, the abundance of pendant groups on hydrogel polymers offers tailorable charge polarities and provides substantial dissociable ions. Due to the extraordinary versatility of hydrogels, they have been used as polyelectrolytes, functional surface layers for the electrodes, water retention or absorption layers, and even ion-selective channels. In the following section, the recent advances in hydrovoltaic technologies using hydrogel materials are reviewed and discussed. It is worth noting that the operating hydrovoltaic devices are accompanied by exchanging the moisture/water with the surrounding environment, along with the transition of the materials from the dehydrated state to the hydrated state or vice versa. The nanomaterials, e.g., protein nanowires and biological nanofibrous composed of hydrophilic polymers that can swell and retain water, are included in this discussion as one type of derived hydrogel materials.

Moisture-enabled electric generator with hydrogel polyelectrolyte
Many research endeavors have been devoted to the energy transduction from moisture (or humidity) gradient to electricity because the gas-liquid moisture is omnipresent in the air and involved in myriad natural and daily events. The first generation of moisture-enabled electric generators (MEGs) made of graphene or its derivatives was invented by Zhao *et al.*, and a model of diffusion-osmosis was proposed[88].

Asymmetric moisturizing of the MEG equipped with the pendant groups that can provide dissociable H^+ enables the energy transduction from moisture gradient to electricity. Particularly, H^+ dissociated from oxygen-containing groups of the graphene oxide film during moisturizing, creating a local concentration increase of mobile H^+, which consequently diffused along with the reduction of its chemical potential to the dehydrated part (in the absence of mobile ions) and produced the electric signals [Figure 12B]. Though the maximal voltage output approached 1.5 V[81], the MEGs using graphene derivatives generally suffered from the transient voltage output[89].

The hydrogel materials, serving as polyelectrolytes, were introduced to develop the second generation of polymer moisture-enabled electric generators (PMEGs), which can produce stable DC electricity [Figure 12B][90]. Analogue to thermopower (α) of i-TEs, the equivalent hydropower can be defined as $\beta = \frac{\Delta V}{\Delta RH}$, which depicts the voltage output versus humidity different across two electrodes. Figure 13A shows a schematic illustration of a PMEG consisting of two carbon electrodes, of which the upper one was manufactured with holes (1.2 mm in diameter) for efficient access to moisture and a layer of poly(4-styrensulfonic acid) (PSSA) polyelectrolyte. When the moisture was supplied to the electrode with holes, the PSSA that possessed rich sulfonated functional groups absorbed the moisture, where a large amount of mobile H^+ was released from the PSSA polymer [Figure 13B]. Inhomogeneous distribution of water molecules across the PSSA corresponded to the concentration gradient of mobile H^+, inducing the diffusion of protons and creating the resultant (open-circuit) voltage of ~0.8 V, corresponding to a β of 1 V (per 100% RH) [Figure 13C], and (short-circuit) current of ~0.1 mA cm^{-2}. Production of stable DC electricity in the PMEG offered the additional practical merit of not needing axillary rectifier circuits. Simply connecting six PMEG units in series can power a LED bulb (with voltage and current requirements in the range of 1.6-2.5 V and 30-100 μA) [Figure 13D]. Besides, the design of the PMEG can be applied to other hydrogel materials, such as PVA, polyacrylic acid (PAA), hydroxyethyl cellulose, Nafion, guar gum, and alginate sodium that contains at least one hydrophilic and polar pendant group, such as hydroxyl, carboxylic, and sulfonic acid. Furthermore, heterogeneous moisture-enabled electric generators (HMEGs) were proposed to improve the electric output by employing a bilayer of polyelectrolyte films[6]. A polycation layer of poly diallyl dimethyl ammonium chloride (PDDA) and a polyanion layer of both polystyrene sulfonic acid (PSS) and PVA (PSSA hybrid) were integrated [Figure 13E]. During moisturizing, the PDDA film and PSSA hybrid film provided dissociated negatively charged Cl$^-$ and positively charged H^+, respectively. Whereafter, dual charge carriers of Cl$^-$ and H^+ diffused with respect to reducing the chemical potential; surprisingly, both cation and anion fluxes could overcome the junction between PDDA and PSSA and therefore establish the heterogeneous charge distribution. An increased voltage of ~0.95 V for about 258 h at a low RH of 25% was achieved. Benefiting from the fabrication ease of the bilayer of polyelectrolyte films and their mechanical flexibility, 1,600 HMEG units can be connected in series via an aligned stacking strategy to reach a voltage of 1,000 V [Figure 13F-H].

Similarly, an ionic hydrogel moisture electric generator (IHMEG) made of PVA-phytic acid (PA)-glycerol hydrogel was developed[91]. A PA with six esterified phosphoric acid groups perfectly served as the proton donor and supplied massive dissociable protons while sufficient water uptake was afforded by hygroscopic glycerol [Figure 14A]. Since the moisture barrier substrate at the bottom of the IHMEG caused asymmetrical moisture absorption across two electrodes [Figure 14B], there was a higher concentration of dissociated H^+ at the top, which consequently diffused to the bottom for the reduction of its chemical energy. Notably, the strong water absorption capability achieved by introducing glycerol and weak hydrogen bonds within the IHMEG hydrogel jointly promoted continuous ion dissociation and ion transport. As a result, a single IHMEG unit of 0.25 cm^2 attained a stable DC voltage of ~0.8 V (referring to a β of about 1 V per 100% RH) for more than 1,000 h and a DC current of ~9 μA for over 20 h [Figure 14C].
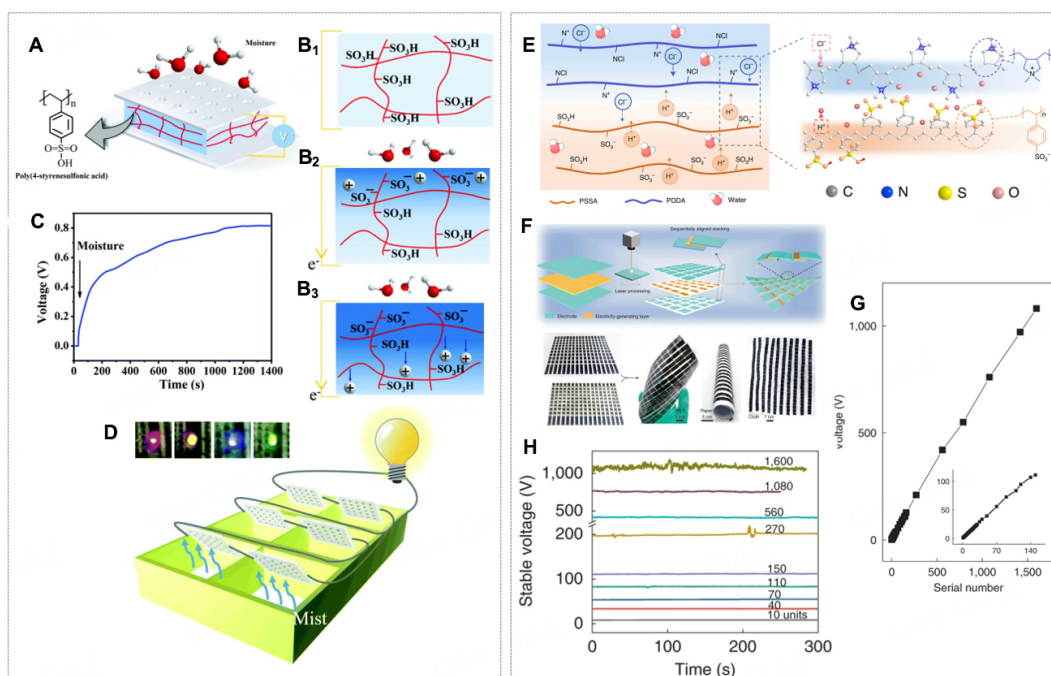
Figure 13. (A) Scheme of a PMEG comprising a PSSA membrane and two gold electrodes. (B_1-B_3) The proposed mechanism of the PMEG. Up: The homogeneous distribution of the functional groups. Middle: Incoming moisture ionized the PSSA membrane and released the protons from the polymer chains. Down: The ionized protons migrated to the other side, leaving the negatively charged polymer chains. (C) V_{oc} detected on a PMEG (1×1 cm^2) at constant moisture. (D) A mist-powered light system where each LED bulb was powered by six flexible PMEG units connected in series. (E) Schematic of a HMEG with a bilayer of polyelectrolyte films (BPF), which enabled spontaneous water adsorption and ion dissociation in moist air. Based on this heterogeneous structure, mobile Cl$^-$ and H$^+$ ions diffused in opposite directions. (F) Schematic of a large-scale integration of HMEG units by sequentially aligned stacking strategy and photographs of flexible HMEGs. (G) Plot of voltage output with different serial numbers of HMEG units. Inset is an enlargement of serial numbers ranging from 1 to 140. (H) Stable voltage signals of the integrated device with 10, 40, 70, 110, 150, 270, 560, 1,080, and 1,600 units in series. (A-F) Reprint with permission from Ref.[90]. Copyright 2019 The Royal Society of Chemistry. (E-H) Reprint with permission from Ref.[6]. Copyright 2021, The Author(s), Springer Nature.

Constructing an intrinsic gradient of dissociable ions inside the hydrogel materials is another way to utilize liquid-gas moisture when exposed to moisture uniformly. For instance, hygroscopic polypyrrole (PPy) was used because of its ability to absorb water from ambient air and 3D microporous structures, in which lithium perchlorate (LiClO$_4$) (in solution) was doped through an electrochemical method[92]. To apply a bias voltage of 3 V to a 3D PPy framework, the positive side was oxidized, forming the concentration gradient of ClO$_4^-$ from the positive electrode (high) to the negative electrode (low). When the entire device was exposed to the moisture uniformly, the ingress of water molecules in 3D PPy led to the breaking of the ionic bond between Li$^+$ and ClO$_4^-$, making mobile Li$^+$ and localized ClO$_4^-$ [Figure 14D]. Since the bottom of 3D PPy framework was heavily doped by LiClO$_4$ with more mobile Li$^+$ generated during moisturizing, Li$^+$ diffused from the high concentration side to the low concentration side, and the voltage output of ~0.06 V and current of 10 μA cm^{-2} was achieved [Figure 14E and F].

Hydrogel-based surface functional layer for a hydrovoltaic generator
In the aforementioned MEGs, the hydrogel materials work as quasi-solid-state polyelectrolytes, donating the mobile unipolar ions while sufficient water uptake is acquired. Such processes yield long-distance ion diffusion with respect to the concentration gradient. The response time of electric signals could be estimated as follows: $L_D = \sqrt{Dt}$, where L_D is the diffusion length. D and t express the diffusion coefficient and time, respectively[93]. Take protons in Nafion as an example: the time for the proton to have a transmembrane
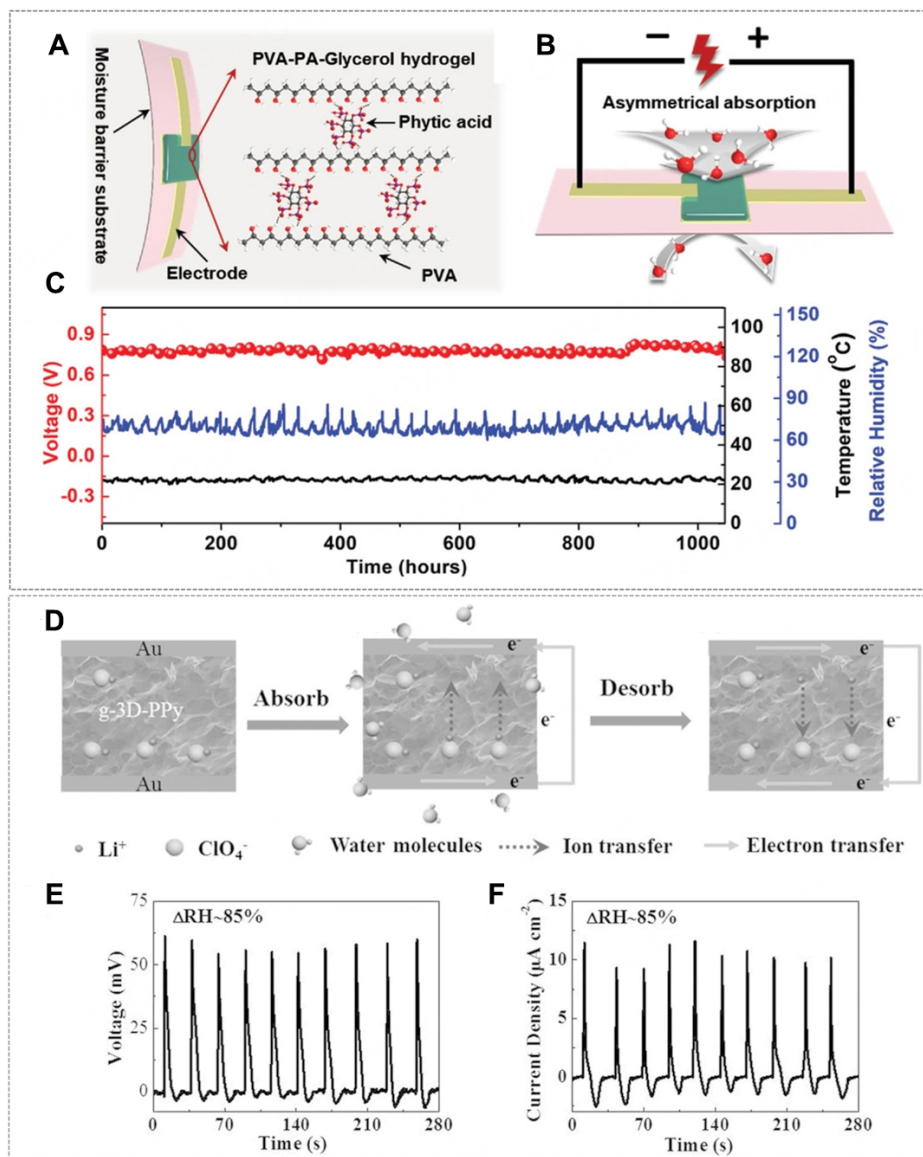
Figure 14. (A) Schematic of an IHMEG device and its functional components. (B) Schematic of the asymmetric moisture stimulus-induced potential in an IHMEG. (C) V_{oc} (red curve) of an IHMEG device over time under an open ambient environment. The ambient relative humidity (blue curve) and temperature (black curve) were synchronously recorded. (D) Left: Schematic of the gradient distribution of ClO_4^- in gradient-3D-PPy. Middle: Free Li^+ ions were ionized by adsorbed water vapor and caused a density gradient of Li^+ ions. Right: In the desorption process of water vapor, the recombination of Li^+ ions and ClO_4^- reduced the potential, resulting in a reverse electron flow in the external circuit. (E and F) voltage and current of the g-3D-PPy framework in response to a periodic RH variation ($\Delta RH = 85\%$). (A-C) Reprint with permission from Ref.[91].Copyright 2022, The Authors, Wiley-VCH. (D-F) Reprint with permission from Ref.[92].Copyright 2016, Wiley-VCH.

diffusion in a dehydrated Nafion is at the order of 10^{-8} cm² s^{-1}[94], which could only be reduced on the condition of wetting the Nafion and increasing its diffusion coefficient. Consequently, the sluggish ion movement involved in MEGs limits the electric output and imposes restrictions on their practical applications. The newly designed hydrogel-based composite demonstrated another strategy to significantly enhance the electric outputs in terms of both voltage and response time[9]. As shown in Figure 15A, the ionic polymer-hydrogel-carbon composite (IPHC) is comprised of ionic polymers of Nafion, pNIPAm hydrogel, and carbon electrodes. Instead of a polyelectrolyte, the hydrogel layer of pNIPAm was the surface function
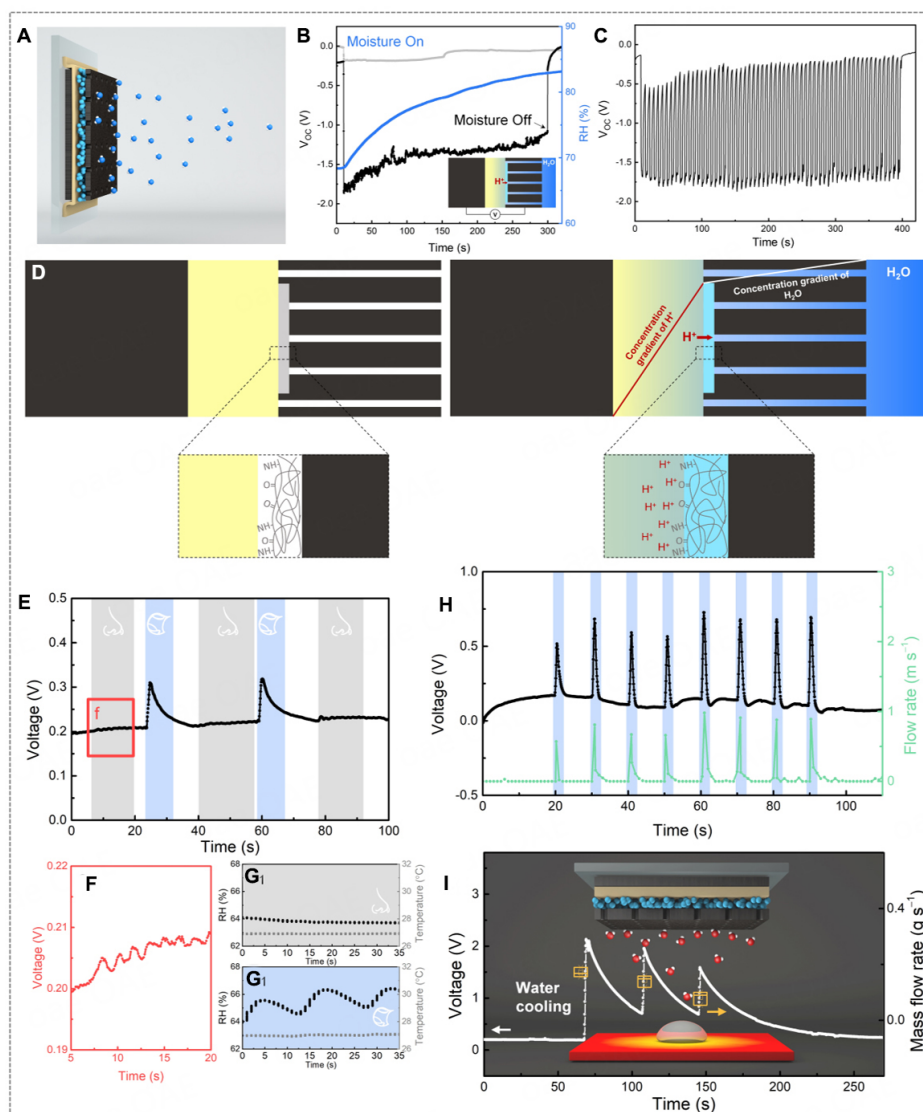
Figure 15. (A) Schematic of an ionic polymer-hydrogel-carbon composite (IPHC) device. (B) V_{oc} of an IPHC and corresponding RH profile in response to moisture flow. (C) Intermittent supply of moisture flows (every 3 s) to an IPHC device and its voltage output. (D) Left: Schematic of an IPHC in the initial dry state. From left to right is carbon paper, Nafion, pNIPAm, and pored carbon paper. Right: in response to moisture flow, the concentration gradient of H_2O and H^+ is built across the IPHC. (E) Voltage signals recorded by the IPHC corresponding to human breath through nose and mouth. (F) Magnified figure of the red-square region in (E). (G) Change in relative humidity (black curve) and temperature (grey curve) for (G_1) nasal breathing and (G_2) mouth breathing. (H) Voltage signals and flow rates when the moisture spray was applied to an IPHC intermittently. (I) Voltage signals of an IPHC in response to the moisture flow generated simultaneously with cooling a hot steel sheet through the water. Reprint with permission Ref.[9]. Copyright 2022, The Royal Society of Chemistry.

layer, which empowered the carbon electrode with a strong binding affinity to protons and largely improved the interfacial kinetics for the chemisorption of protons. When the moisture gradient was created by supplying moisture flow to the IPHC, the pNIPAm became swollen; meanwhile, the portion of small water droplets carrying adequate kinetic energy was imbibed by the Nafion membrane. The dissociated protons from the Nafion were immediately captured by the pNIPAm-graft carbon electrode owing to its strong affinity to protons. Such fast chemisorption of protons on the carbon electrode generated a very high voltage of 1.86 V in magnitude and extremely fast electric output [Figure 15B and D]. It was further verified by the supply of intermittent moisture flow every 3 s to the IPHC [Figure 15C]. Benefiting from the high

electric output and fast response, the IPHC was applied in several daily life scenarios. Figure 15E-G shows the voltage response of an IPHC to human breath through the nose and mouth. Only a < 2% change in RH causes the voltage response sensitivity (V_{wet}/V_{dry}) to change by about 1.5, demonstrating the unforeseen opportunity for IPHCs to be used for medical purposes to identify patients with rhinitis who suffer from abnormal nasal breathing and can only breathe through the mouth. Moreover, the IPHC can respond to the moisture flow that was created mechanically in high-pressure water atomization processes and water-cooling processes [Figure 15H and I].

Hygroscopic media for hydrovoltaic generators

Beyond artificially supplying moisture or placing the hydrovoltaic device in a high humidity environment, the hygroscopic materials, including biological polymers and the combination of hydrogel with hygroscopic salts, enable the hydrovoltaic alternatives, which are less dependent on a liquid water source and can work spontaneously to capture the moisture from the air. Thus, the operating window in terms of the RH range and scope of application can be extended. For instance, a thin film of hygroscopic protein nanowires gained from the microorganism G. sulfurreducens was reported to exhibit continuous voltage output of 0.4-0.6 V for over 2 months at the RH of 40%-50% [Figure 16B][95]. Such a device abided by the same electricity generation principle as most MEGs, i.e., the transduction of a moisture gradient to a concentration gradient of dissociated charge carriers. As only the protein nanowires at the top surface were able to access and capture the moisture in the air, a vertical moisture gradient was built from the tiny gold electrode at the top to the large gold electrode at the bottom, which was completely insulated from the ambient air [Figure 16A]. The protein nanowires possessed abundant carboxylic groups where the diffusion of free protons against the immobile COO⁻ anionic background was responsible for the observed voltage. It was important to design a proper thickness of protein nanowires where the entire film was within the interfacial vapor-pressure gradient and retained a dynamic equilibrium of water adsorption-desperation exchange at the interface[96]. Therefore, the moisture penetration rate was pretty slow, and the penetration depth was inversely proportional to the film thickness [Figure 16C-E]. The protein nanowires of about 10 μm ensured a stable moisture gradient across the device, and the long-term stability of electric output was preserved. Additionally, various configurations of the device, such as the horizontal configuration with the left electrode exposed to the air, were developed to further verify the correlation between the direction of the moisture gradient and the voltage signals [Figure 16F].

The hydrogels were also infused with hygroscopic salts to harvest moisture in the air. For instance, the carbon substrate made of carbon black nanoparticles was partially coated with PVA hydrogel containing sodium chloride (NaCl) to fabricate an asymmetric hygroscopic structure (AHS) [Figure 16G][97,98]. By absorbing water from the air, wet-dry asymmetry was developed across the carbon substrate, where the surface potential of wet carbon decreased [Figure 16H]. The EDLs were then formed with Na⁺ ions adsorbed on the carbon substrate, and such cations aggregated at the contact interface (i.e., wet-dry interface) led to the observed electric outputs [Figure 16I-K]. Especially owing to the high viscosity of this ionic hydrogel, it prevented the interior water from passing across the wet-dry boundary to maintain a long-lasting lateral wet-dry interface, contributing to a V_{oc} of ~0.6 V for over 150 h [Figure 16L]. Furthermore, the hygroscopic hydrogel can serve as the transport media for the charge carriers. A moisture-induced self-charging device (MISD) was fabricated, which consisted of two lateral carbon nanotube electrodes bridged by hydrochloric acid (HCl)/PVA hydrogel with calcium chloride ($CaCl_2$) on one side [Figure 16M][99]. The device's self-charging process was performed by absorbing water and forming a local $CaCl_2$ solution, which diffused into HCl/PVA hydrogel and caused the diffusion of cations from the $CaCl_2$ side to the other. Interestingly, the authors reported that the transport of cations was selectively facilitated against the anions of Cl⁻ owing to the asymmetric interactions of $CaCl_2$ with HCl/PVA hydrogel. The HCl/PVA played a role in regulating the diffusion coefficients of cations and anions. The cation flux and its accumulation produced
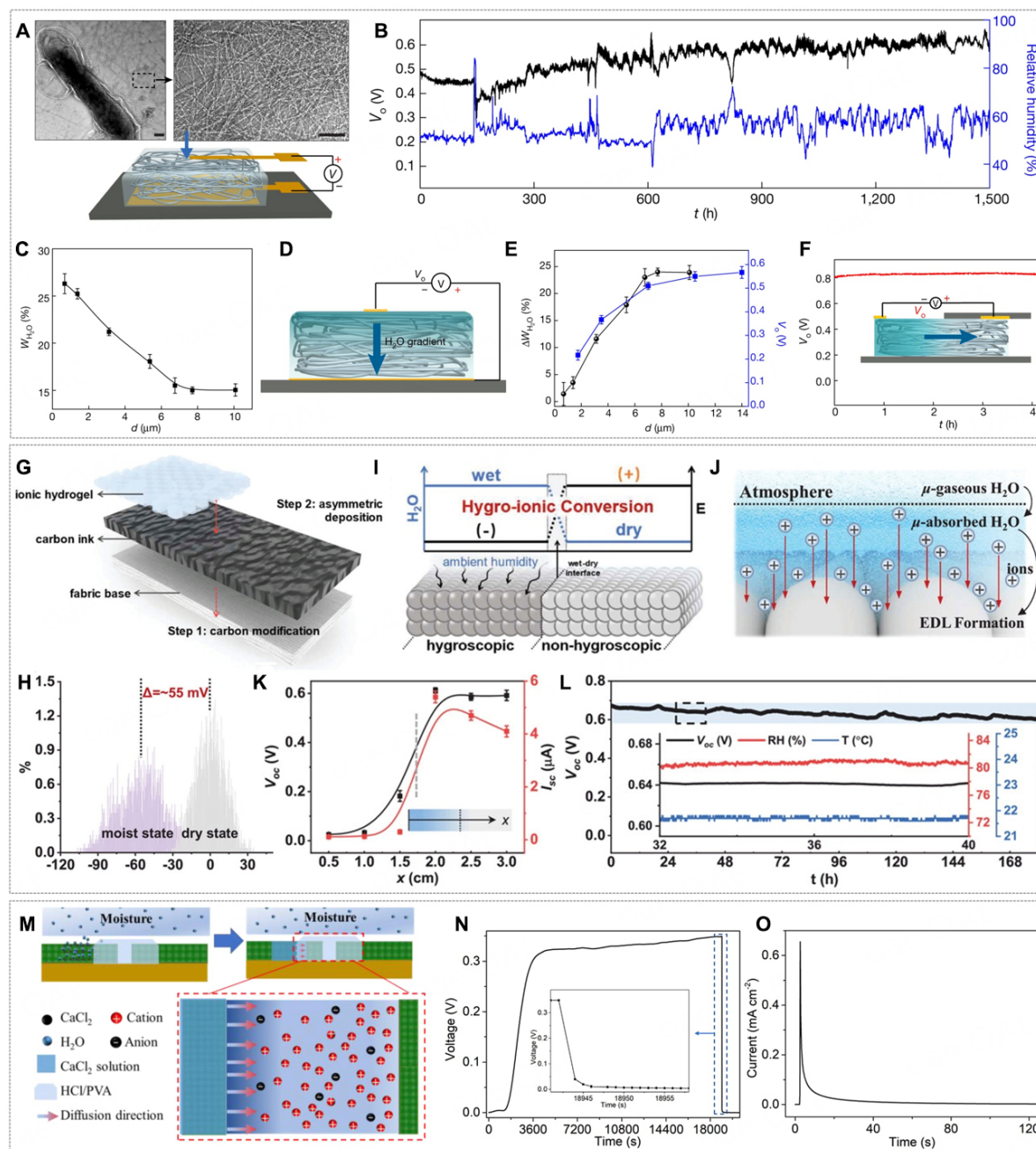
Figure 16. (A) Top: Transmission electron microscope images of the purified protein nanowires. Scale bars, 100 nm. Bottom: diagram of the device. (B) A continuous recording of open-circuit voltage from a device for more than two months. (C) The moisture adsorption ratio (W_{H2O}) in nanowire films is plotted against film thickness (d) at an ambient RH of roughly 50%. (D) Diagram showing a vertical moisture gradient in the nanowire film. (E) ifference in moisture adsorption (ΔW_{H2O}) and output voltage plotted against d. (F) A residual open-circuit voltage of about 0.8 V was measured from a pair of top electrodes in a nanowire device with half of the top surface covered by a glass slide. (G) Schematic of the structure and fabrication process of the AHS. (H) Surface potential distributions of the AHS. (I) Schematic of the wet-dry interface in an AHS after water absorption. (J) Energy conversion pathways in the AHS based on cations adsorption on carbon surface for EDL formation. (K) The correlation between V_{oc}, I_{sc} and the measuring distance (x) between wet-carbon and dry-carbon. (L) V_{oc} of an AHS under constant ambient conditions. (M) Schematic of the moisture-induced self-charging mechanism. (N) V_{oc} and (O) I_{sc} of the device. (A-F) Reprint with permission Ref.[95]. Copyright 2020, The Author(s), Springer Nature. (G-L) Reprint with permission Ref.[97]. Copyright 2022, Wiley-VCH GmbH. (M-O) Reprint with permission Ref.[99]. Copyright 2019, Elsevier.

a voltage of 0.348 V at RH of 80% and a transient current [Figure 16N and O]. The water uptake of $CaCl_2$ grew to saturation and would lead to the decay of voltage after 1 h.

Selective ion transport media for a hydrovoltaic generator

The evaporation-driven water flow enables another type of hydrovoltaic technology where a classic electrokinetic mechanism of streaming potential is applied[69,100,101]. Such hydrovoltaic devices are equipped with the charged nanochannels or nanopores in the structure and hydrophilic pendant groups on a polymer backbone, where water uptake occurs at the inlet because of either hydrophilic absorption or capillary force, and then water flows through the material and evaporates at the outlet. For example, Figure 17A shows the voltage responses (up to 110 mV) of the hydrovoltaic devices made by several types of biological nanofibrous (NFs), including cellulose, chitin, silk, and lysozyme[100]. The as-prepared NFs were subject to directionally freezing to form the structure with oriented microchannels (1-10 μm) and nanopores (2-50 nm) [Figure 17B], and these NFs were endowed with different polar groups (such as carboxy groups and quaternary ammonium groups) and exhibited a large difference in zeta potential [Figure 17C]. A great number of ions were dissociated from the polar functional groups of the NFs during the ingress of water and started to move along with the water flow driven by rapid water evaporation. Among the NFs, the electrical double layers of opposite sites were overlapped properly; thus, the channels were filled with a close to a unipolar solution of counter-ions[102], allowing the selective ion transport [Figure 17D]. Hence, such an ion flux across the NFs contributed to the streaming potential [Figure 17E]. Moreover, the voltage output would be jointly controlled by the RH, velocity of airflow, and zeta potential of the NFs. Similarly, the cellulose nanofibre can be functionalized by a metal-organic framework of $Ni_3(2,3,6,7,10,11-$hexaiminotriphenylene$)_2$ (Ni-HITP) [Figure 17F and G], which enabled light absorption for water evaporation and allowed H^+ and OH^- doping in acid and alkaline solution, respectively. Thus, such doped surfaces of cellulose nanofibre exhibited different zeta potentials and caused the streaming potential with negative (~-0.3 V) and positive (~0.35 V) polarities during water evaporation [Figure 17H and I][103]. Especially, the solar-thermal driven water evaporation also created a temperature gradient of ~5 °C across the cellulose film with Ni-HITP, corresponding to a thermopower of 8.5 mV K^{-1} [Figure 17J and K]. This work reveals that the water evaporation of hydrogels in an open system (without strict encapsulation) might lead to both hydrovoltaic and thermoelectric power generation, which therefore needs careful study to distinguish the major contribution. Instead of selective ion transport media, hydrogels can be used as water reservoirs with an excellent water retention capability and hydrophilic binder to operate collectively with other surface-charged frameworks[69].

Challenges for hydrogel-based hydrovoltaic devices

Although significant enhancements in electric outputs (i.e., voltage, current, or power density) have been achieved in different hydrogel-based hydrovoltaic devices, the understanding of their electricity generation mechanisms is in the infant stage. Specifically, for the charging process (i.e., voltage generation), most hydrovoltaic devices convert the moisture gradient into the concentration gradient of ions in the electrolyte, which shares a similar mechanism to TDCs that are governed by temperature-induced ion transport (e.g., the Soret effect). The asymmetric distribution of cations or anions is responsible for the observed voltage. However, for the discharging process (i.e., current production through external loads), there is still a lack of justified models. The ions in the electrolyte are not able to pass the electrolyte/electrode boundary; that is the reason most TDCs undergo a 4-stage cycle in order to give a discharging current and useful power. Consequently, TDCs were limited to an intermittent working mode (as discussed in Section "INTRODUCTION"). It should be noted that several hydrovoltaic devices worked continuously to produce current and power without going through the cycle. But unfortunately, most studies neglected to explain the reasons. Taking the materials of electrodes (e.g., carbon, gold, and platinum) into consideration[9,90,95,100], faradic redox reactions at the electrode surface could be ruled out. To understand such elusive phenomena,
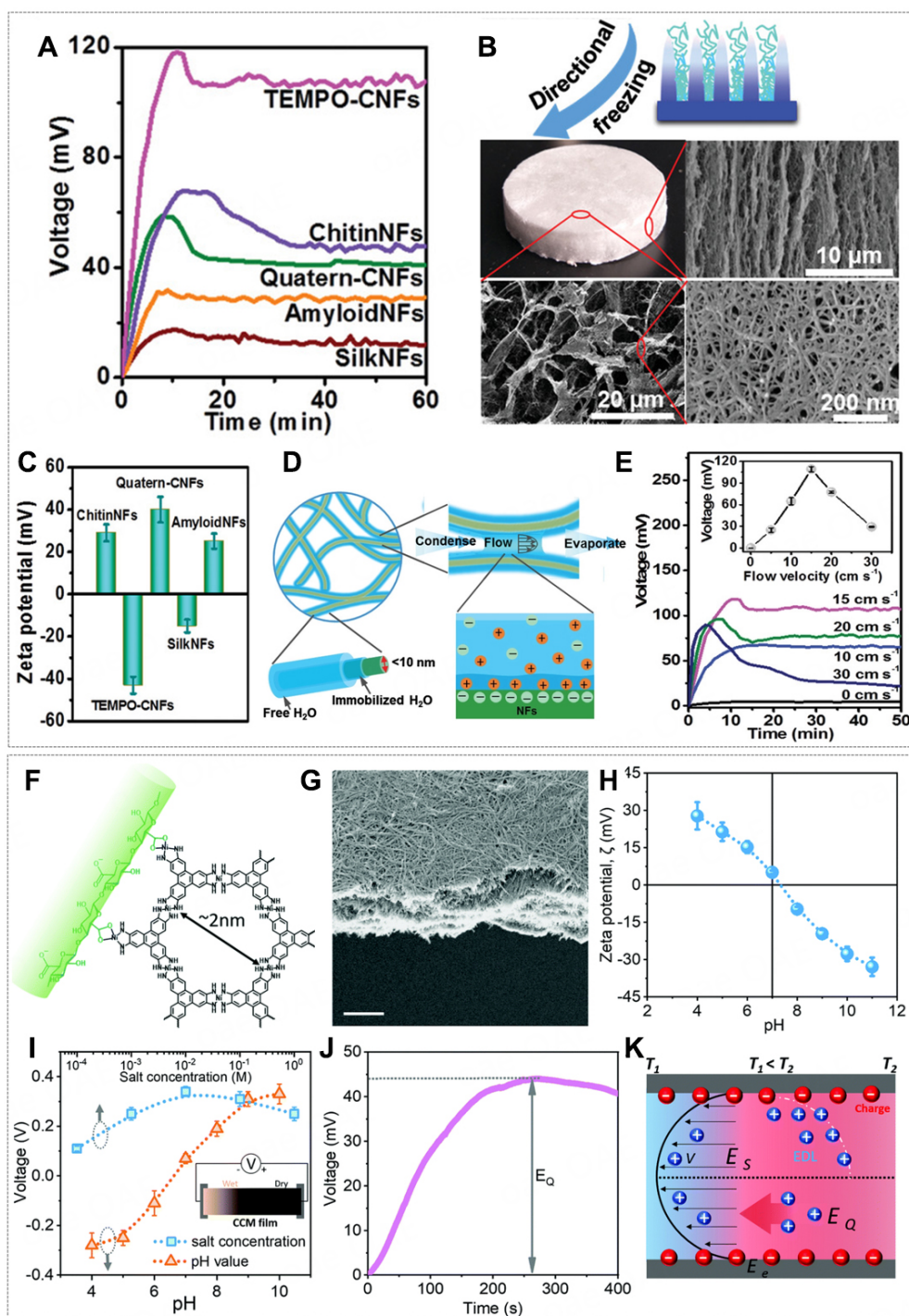
Figure 17. (A) V_{oc} generated by biological generators made of different nanofibrils (NFs). (B) Optical and scanning electron microscope images of aerogel fabricated by directionally freezing. (C) Zeta potentials of biological NF dispersions. (D) Schematic of hydrated channels around and between NFs. (E) V_{oc} variation upon exposure to airflow with different velocities. (F) Structure of the conductive metal-organic framework layered on cellulose nanofibre and the assembled film. (G) Cross-sectional scanning electron microscopy image of the film. Scale bar, 5 μm. (H) Measured zeta potentials of the cellulose nanofibers at different pH values. (I) The streaming potential generated in the hybrid cellulose nanofibre @ conductive metal-organic framework film at different pH (where the NaCl concentration was fixed at 0.01 M) and different salt concentrations (where the pH value was fixed at 10). (J) The measured ionic thermoelectric voltage at a temperature gradient of 5 °C. (K) A schematic of ion distribution and transport in the charged nanochannels and the proposed mechanisms for voltage generation. (A-E) Reprint with permission Ref.[100]. Copyright 2019, Wiley-VCH. (F-K) Reprint with permission Ref.[103]. Copyright 2021, The Royal Society of Chemistry.

more systematic and careful studies and reliable theories are needed. Moreover, there is likely a trade-off between voltage and current output as most devices were either limited by a small current or a low voltage. The actual power output through the external loads poorly matched the projected value of maximal power density. The valid method of evaluating power density for different systems abiding by various working mechanisms or working modes (i.e., continuous or intermittent) also requires further study.

In practical terms, there is plenty of scope for maximizing electric output and optimizing hydrovoltaic design. Engineering the hydrogel with desirable function groups and controlled nanostructures allows us to tune the water absorption/desorption kinetics and upgrade charge separation capability, which is promising to promote the voltage output, response time, and charge capacity. On the other hand, the continuous and stable electric output in terms of both voltage and current is required to secure a continuous working mode and avoid energy loss in auxiliary rectifier circuits. The gradient energy conveyed by water molecules and ions needs to be fully transferred to the solid electrodes to truly appreciate massive hydrovoltaic energy. Some redox-active electrodes, such as silver/silver chloride, PANI, could be adapted to convert an ion current in liquids to an electron current in the lead wire at the electrode/electrolyte boundary with the occurrence of faradic reactions. Integrating hydrogel polyelectrolytes with conductive hydrogel electrodes is of practical importance in pursuing flexible and wearable hydrovoltaic units.

HYDROGEL-BASED THERMO-WATER COGENERATION

Considering a (photo)thermal energy-water nexus, the spontaneity and universality of water evaporation in hydrogel materials and symbiotic temperature regulating and conduction events imply precious opportunities to integrate thermoelectric and hydrovoltaic units for optimizing energy recovery. Also, the structure conformability of hydrogel materials offers extra merits for pairing up different thermoelectric and hydrovoltaic modules.

For example, a photothermal steam and electricity cogeneration was reported, which had a layer-by-layer structure of PAm hydrogel, polydimethylsiloxane (PDMS) polymer film, bilateral copper oxide/copper foil (CuO/Cu) electrodes, and a cupric sulfate ($CuSO_4$)-PAm hydrogel electrolyte [Figure 18A][10]. Each layer was individually addressed in terms of thickness, composition, and functionality. The outer shell of the PAm hydrogel facilitated a constant supply of water for the whole device, and the inner PAm hydrogel was furnished with a redox-active $CuSO_4$ electrolyte. The nanostructured CuO/Cu electrodes were responsible for the thermogalvanic effect and photothermal effect, by which a temperature gradient across the space between the hot upper CuO/Cu solar absorber and cold bulk water was attained. The PDMS wrap played multiple roles to ensure good contact between the electrodes and the hydrogel electrolyte, prevent the dehydration of the electrolyte, and offer a hydrophobic surface and self-floating capability. As a result, the maximum T of about 8.7 °C and V_{oc} of about 10.3 mV were obtained under one sun irradiation, corresponding to a thermopower of 1.2 mV K^{-1}, and the peak output density reached 1.57 mW m^{-2} [Figure 18B and C]. In addition, the regeneration of CuO/Cu could be performed by reversing the device [Figure 18D]. Likewise, the PAm hydrogel that contained a redox couple of $K_4Fe(CN)_6$/$K_3Fe(CN)_6$ and lithium bromide (LiBr) obtained a thermopower of -1.2 mV K^{-1}, where two thermodynamic processes, i.e., thermogalvanic effect and water phase transition, worked collectively [Figure 18E-G][70]. Particularly, a high concentration of 5.4 M LiBr in PAm hydrogel alerted its saturated vapor pressure, so the PAm hydrogel could be chilled by water evaporation at 50 °C and absorb the water from the surrounding air for self-regeneration at 25 °C.

Assembling a hydrovoltaic generator relying on water evaporation and hydrogel-based TGC can bring twofold thermal benefits: escalating the temperature for efficient water evaporation and chilling the cold
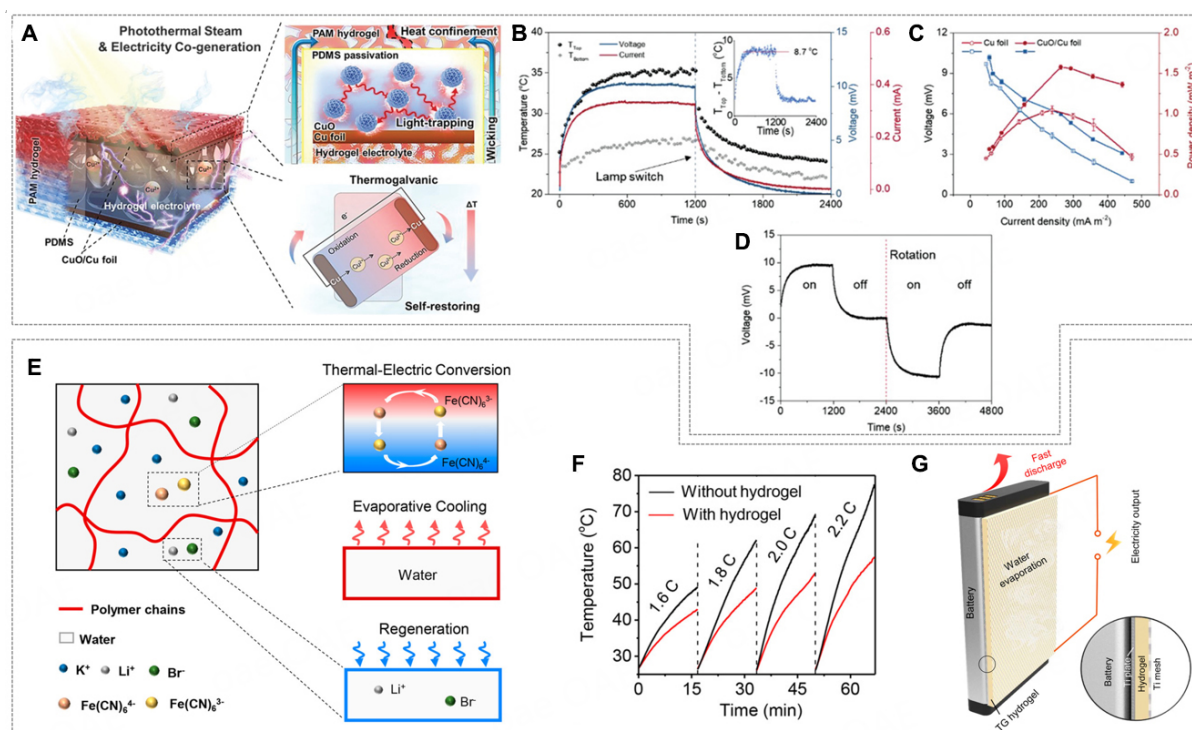
Figure 18. (A) Schematic of the designed integrative photothermal evaporator/thermogalvanic cell. (B) Temperature profiles of the upper and bottom surfaces under chopped one sun illumination and corresponding V_{oc} and I_{sc} (inset: temperature difference between two surfaces). (C) Discharge polarization curves and related power densities of the thermogalvanic cells using Cu foil or CuO/Cu foil as electrodes. (D) V_{oc} of this cell with cycle rotation. (E) Schematic of the structure and working principle of the smart thermogalvanic hydrogel. (F) Temperature variation of the battery at different discharging rates with (red) and without (black) thermogalvanic hydrogel on the surface. (G) Schematic of the experiment setup. Inset shows the cross-sectional view. (A-D) Reprint with permission Ref.[10]. Copyright 2020, Wiley-VCH. (E-G) Reprint with permission Ref.[70]. Copyright 2020, American Chemical Society.

electrode in TGC. A heat conduction effect enhanced hydrovoltaic power generator (HCEHG) was reported. It was comprised of an i-TE made by gelatin and $K_4Fe(CN)_6/K_3Fe(CN)_6$ and a hydrovoltaic module of porous dual-size Al_2O_3 (d-Al_2O_3)[11]. As for the TGC module, in the absence of an artificial temperature control system, a temperature gradient of about 2 K was built from right to left [Figure 19A], where the hot carbon fiber electrode was heated directly by sunlight, and the cold electrode was automatically cooled with the aid of water evaporation in the hydrovoltaic module. A thermal voltage (~1 mV) was generated via the thermogalvanic effect of the $K_4Fe(CN)_6/K_3Fe(CN)_6$ redox couple. The water gradient in the hydrovoltaic module was built from bottom to top. By virtue of positively charged nanochannels inside d-Al_2O_3 and the heat gained from the TGC module, the voltage output was increased from 3.4 V (without TGC) to 4.0 V [Figure 19B and C] along with the upstreaming flux of hydroxyl ions.

Additionally, the thermo-diffusion of water (not ionic species) in the polyelectrolyte presents another strategy for thermo-hydro-electrochemical power generation in a neat fashion. Zhang *et al.* reported a device made of hygroscopic polyelectrolyte of polyaniline and polystyrene sulfonate (PANI:PSS) and carbon steel electrodes, from which an ultrahigh thermopower of -93 mV K^{-1} was achieved [Figure 19D][104]. The PANI:PSS polyelectrolyte absorbed about 15 wt% water from the ambient environment with an RH of around 50%, and the diffusion of water from the hot side to the cold side ensued under a temperature gradient. The asymmetric water distribution caused the shifts of overpotential for carbon steel corrosion [Figure 19E and F]. Explicitly, higher (lower) water concentration led to a decreased (increased) overpotential. Such a water gradient was converted into the voltage with respect to the thermal bias. Moreover, the corrosion of the carbon steel was surprisingly slow and yielded only about 18 μm for six months.

Figure 19. (A) Schematic of the structure and mechanism of the heat conduction effect enhanced hydrovoltaic power generator (HCEHG) for sustained evaporation electricity output and thermoelectric conversation. (B) V_{oc} the hydrovoltaic module with and without the thermoelectric module. (C) Real-time temperature plots of the surfaces of the dual-size Al_2O_3 hydrovoltaic module and thermogalvanic module and corresponding temperature difference. The ambient temperature is ~290.4 K. Grey areas indicate that the device is illuminated. (D) Voltage profile of the device with the fully developed oxidation layer under 50% RH as a function of time when the temperature difference was altered. The inset shows the saturated voltage at the corresponding temperature to seek the slope (93 mV K^{-1}). Note it has the opposite sign (-93 mV K^{-1}) based on Equation 1 in this work. (E_1-E_4) Illustration showing thermoelectric voltage generation and the corresponding potential changes in the hotter and colder sides. Top left: Uniformly distributed water in PANI:PSS under $\Delta T = 0$. Top right: As $\Delta T > 0$, water molecules migrated from the hotter to the colder side. Bottom right: Voltage generation at steady state under $\Delta T > 0$. Bottom left: Water molecules returned to their initial distributed states under ΔT approaching 0. (F) Evans diagram shows the cathodic-reduction reaction (black line), and the anodic oxidation reaction (greenish line) under uniform temperature. The greenish line shifts toward the red (or blue) line with less (or more) water on the electrodes. (A-C) Reprint with permission Ref.[11]. Copyright 2022, The Author(s), Springer Nature. (D-F) Reprint with permission Ref.[104]. Copyright 2021, The Author(s), Springer Nature.

CONCLUSIONS AND OUTLOOK

In this review, the recent progress of i-TEs and hydrovoltaic devices using hydrogel materials has been discussed. Owing to the molecular-level tailorable features of hydrogel polymers and their interactions with water and other functional additives, hydrogels provide an ideal platform for low-grade heat and water energy harvesting from both fundamental and practical perspectives. Versatile hydrogels have been successfully employed in i-TEs, hydrovoltaic devices, and their hybrids as polyelectrolytes, transport media, separators, ion channels, surface functional layers, and more, making big strides forward in the transduction of gradient energy into electricity. Hydrogel-based i-TEs have improved thermopower from a few hundred μV K^{-1} to tens of mV K^{-1} at a low-grade heat range, and hydrogel-based hydrovoltaic devices even achieved the hydropower of 1 V per 100% RH and even higher. Such significant electric output is of practical importance for portable energy recovery systems for daily use without the need for auxiliary amplifying and rectifying circuits and capturing scattered heat sources and water sources around us. Nevertheless, there are still many challenges involving unknown working mechanisms that remain to be properly addressed in the

future. Overall, current studies of i-TEs and hydrovoltaics are largely based upon empirical studies, but the vast majority of studies have been qualitative. In order to truly appreciate the advances of hydrogel-based gradient energy transduction systems, it is vital to apply more advanced characterization tools and *in-situ* techniques to observe and understand microcosmic interactions among water, polymers, and ionic species, from which the guidelines of hydrogel selection and optimal design could be deduced. Besides, bulk ion transport, local drifting of ions, interfacial ion accumulation, and redox processes all occur at different length scales. A systematic investigation is needed to build the connection between microscopic characteristic behaviors and macroscopic properties and performances. Moreover, the valid and predictable model of evaluating power density for different systems abiding by various working mechanisms or working modes also requires further study. Specifically, the power density of i-TEs and hydrovoltaic devices basically determines their application and deployment in practice, which, however, is one order lower than some nanofluidic devices (a few W m^{-2}) using gradient energy of salinity gradient[99]. Take hydrogel-based i-TEs as an example, the highest power density that can be achieved by a single module is 0.66 mW m^{-2} K^{-2}[18]. There is still a gap for a single device to achieve practically useful power. Future efforts could be implemented on developing stimuli-responsive hydrogels for enhanced thermoelectric performance, in which the responsive hydrogel selectively coordinates with redox couple and regulates the local concentration ratio of C_{Red}/C_{Ox} at different temperatures. This molecular scale responsiveness has the potential to overcome the limited thermopower governed by specific redox couple and corresponding reaction entropy. In addition, other properties of hydrogel materials, including mechanical strength, dimensional stability, water retention capability, anti-freezing capability, and durability under harsh conditions, should be focused on to meet the criteria for real applications. The newly designed hydrogel-based low-grade energy harvesters are expected to open new horizons for extensive applications in the future with their superiorities, including excellent electric outputs, ease of manufacturing, and customizable geometry shape, as well as broad operating range in the ambient environment.

DECLARATIONS

Author Contributions
Initiated this review: Liu C, Fang NX
Wrote the manuscript: Liu C, Wang S
Provided input for discussions and proofreading: Feng SP

Availability of data and materials
Not applicable.

Conflicts of interest
All authors declared that there are no conflicts of interest.

Ethical approval and consent to participate

Not applicable.

Consent for publication

Not applicable.

Copyright

© The Author(s) 2023.

REFERENCES

1. Conti J. Annual energy outlook 2013 with projections to 2040. technical report DOE/EIA-0383. Washington, DC, USA: The U.S. Energy Information Administration, 2013.
2. Bai J, Huang Y, Cheng H, Qu L. Moist-electric generation. *Nanoscale* 2019;11:23083-91. DOI
3. Quickenden TI, Mua Y. A review of power generation in aqueous thermogalvanic cells. *J Electrochem Soc* 1995;142:3985-94. DOI
4. Wichterle O, Lim D. Hydrophilic gels for biological use. *Nature* 1960;185:117-8. DOI
5. Guo Y, Bae J, Fang Z, Li P, Zhao F, Yu G. Hydrogels and hydrogel-derived materials for energy and water sustainability. *Chem Rev* 2020;120:7642-707. DOI PubMed
6. Wang H, Sun Y, He T, et al. Bilayer of polyelectrolyte films for spontaneous power generation in air up to an integrated 1,000 V output. *Nat Nanotechnol* 2021;16:811-9. DOI PubMed
7. Li T, Zhang X, Lacey SD, et al. Cellulose ionic conductors with high differential thermal voltage for low-grade heat harvesting. *Nat Mater* 2019;18:608-13. DOI PubMed
8. Liu C, Li Q, Wang S, Liu W, Fang NX, Feng S. Ion regulation in double-network hydrogel module with ultrahigh thermopower for low-grade heat harvesting. *Nano Energy* 2022;92:106738. DOI
9. Liu C, Wang S, Wang X, et al. Hydrovoltaic energy harvesting from moisture flow using an ionic polymer-hydrogel-carbon composite. *Energy Environ Sci* 2022;15:2489-98. DOI
10. Meng FL, Gao M, Ding T, Yilmaz G, Ong WL, Ho GW. Modular deformable steam electricity cogeneration system with photothermal, water, and electrochemical tunable multilayers. *Adv Funct Mater* 2020;30:2002867. DOI
11. Li L, Feng S, Bai Y, et al. Enhancing hydrovoltaic power generation through heat conduction effects. *Nat Commun* 2022;13:1043. DOI PubMed PMC
12. Forman C, Muritala IK, Pardemann R, Meyer B. Estimating the global waste heat potential. *Renew Sustain Energy Rev* 2016;57:1568-79. DOI
13. Bell LE. Cooling, heating, generating power, and recovering waste heat with thermoelectric systems. *Science* 2008;321:1457-61. DOI PubMed
14. He J, Tritt TM. Advances in thermoelectric materials research: looking back and moving forward. *Science* 2017;357:eaak9997. DOI PubMed
15. Cheng C, Dai Y, Yu J, et al. Review of liquid-based systems to recover low-grade waste heat for electrical energy generation. *Energy Fuels* 2021;35:161-75. DOI
16. Yu B, Duan J, Cong H, et al. Thermosensitive crystallization-boosted liquid thermocells for low-grade heat harvesting. *Science* 2020;370:342-6. DOI PubMed
17. Zhao D, Wang H, Khan ZU, et al. Ionic thermoelectric supercapacitors. *Energy Environ Sci* 2016;9:1450-7. DOI
18. Han CG, Qian X, Li Q, et al. Giant thermopower of ionic gelatin near room temperature. *Science* 2020;368:1091-8. DOI PubMed
19. Burrows B. Discharge behavior of redox thermogalvanic cells. *J Electrochem Soc* 1976;123:154-9. DOI
20. Quickenden T, Vernon C. Thermogalvanic conversion of heat to electricity. *Solar Energy* 1986;36:63-72. DOI
21. Mua Y, Quickenden TI. Power conversion efficiency, electrode separation, and overpotential in the ferricyanide/ferrocyanide thermogalvanic cell. *J Electrochem Soc* 1996;143:2558-64. DOI
22. Gao C, Lee SW, Yang Y. Thermally regenerative electrochemical cycle for low-grade heat harvesting. *ACS Energy Lett* 2017;2:2326-34. DOI
23. Ding Y, Guo X, Ramirez-meyers K, et al. Simultaneous energy harvesting and storage *via* solar-driven regenerative electrochemical cycles. *Energy Environ Sci* 2019;12:3370-9. DOI
24. Yang Y, Loomis J, Ghasemi H, et al. Membrane-free battery for harvesting low-grade thermal energy. *Nano Lett* 2014;14:6578-83. DOI PubMed
25. Liu Y, Gao C, Sim S, Kim M, Lee SW. Lithium manganese oxide in an aqueous electrochemical system for low-grade thermal energy harvesting. *Chem Mater* 2019;31:4379-84. DOI
26. Cheng C, Wang S, Tan P, et al. Insights into the thermopower of thermally regenerative electrochemical cycle for low grade heat harvesting. *ACS Energy Lett* 2021;6:329-36. DOI
27. Sales BB, Burheim OS, Porada S, Presser V, Buisman CJN, Hamelers HVM. Extraction of energy from small thermal differences near room temperature using capacitive membrane technology. *Environ Sci Technol Lett* 2014;1:356-60. DOI

28.   Lee SW, Yang Y, Lee HW, et al. An electrochemical system for efficiently harvesting low-grade heat energy. *Nat Commun* 2014;5:3942. DOI PubMed

29.   Zhu X, Rahimi M, Gorski CA, Logan B. A thermally-regenerative ammonia-based flow battery for electrical energy recovery from waste heat. *ChemSusChem* 2016;9:873-9. DOI PubMed

30.   Zhang F, Liu J, Yang W, Logan BE. A thermally regenerative ammonia-based battery for efficient harvesting of low-grade thermal energy as electrical power. *Energy Environ Sci* 2015;8:343-9. DOI

31.   Cheng C, Wang S, Wu Y, et al. Thermally regenerative CO_2-induced pH-gradient cell for waste-to-energy conversion. *ACS Energy Lett* 2021;6:3221-7. DOI

32.   Cheng C, Wang S, Wu Y, et al. pH-sensitive thermally regenerative cell (pH-TRC) with circulating hydrogen for long discharging time and high-power output. *Chem Eng J* 2022;449:137772. DOI

33.   Wang X, Huang YT, Liu C, et al. Direct thermal charging cell for converting low-grade heat to electricity. *Nat Commun* 2019;10:4151. DOI PubMed PMC

34.   Mu K, Mu Y, Wang X, et al. Direct thermal charging cell using nickel hexacyanoferrate (II) anode for green recycling of low-grade heat. *ACS Energy Lett* 2022;7:1146-53. DOI

35.   Bard AJ, Faulkner LR. Electrochemical methods: fundamentals and applications, 2nd ed. New York: John Wiley&Sons; 2001. pp. 12-4.   Available   from: https://www.wiley.com/en-us/ Electrochemical+Methods%3A+Fundamentals+and+Applications%2C+2nd+Edition-p-9780471043720 [Last accessed on 21 March 2023].

36.   Ishay JS, Pertsis V, Rave E, Goren A, Bergman DJ. Natural thermoelectric heat pump in social wasps. *Phys Rev Lett* 2003;90:218102. DOI PubMed

37.   Brown BR, Hughes ME, Russo C. Thermoelectricity in natural and synthetic hydrogels. *Phys Rev E Stat Nonlin Soft Matter Phys* 2004;70:031917. DOI PubMed

38.   Siddique ARM, Mahmud S, Heyst BV. A review of the state of the science on wearable thermoelectric power generators (TEGs) and their existing challenges. *Renew Sustain Energy Rev* 2017;73:730-44. DOI

39.   Yang P, Liu K, Chen Q, et al. Wearable thermocells based on gel electrolytes for the utilization of body heat. *Angew Chem Int Ed* 2016;55:12050-3. DOI PubMed

40.   Fang Y, Cheng H, He H, et al. Stretchable and transparent ionogels with high thermoelectric properties. *Adv Funct Mater* 2020;30:2004699. DOI

41.   Lei Z, Gao W, Wu P. Double-network thermocells with extraordinary toughness and boosted power density for continuous heat harvesting. *Joule* 2021;5:2211-22. DOI

42.   Akbar ZA, Jeon J, Jang S. Intrinsically self-healable, stretchable thermoelectric materials with a large ionic Seebeck effect. *Energy Environ Sci* 2020;13:2915-23. DOI

43.   Hu R, Cola BA, Haram N, et al. Harvesting waste thermal energy using a carbon-nanotube-based thermo-electrochemical cell. *Nano Lett* 2010;10:838-46. DOI PubMed

44.   Abraham TJ, MacFarlane DR, Pringle JM. Seebeck coefficients in ionic liquids--prospects for thermo-electrochemical cells. *Chem Commun* 2011;47:6260-2. DOI PubMed

45.   Liu C, Lee H, Chang YH, Feng SP. The study of electrical conductivity and diffusion behavior of water-based and ferro/ferricyanide-electrolyte-based alumina nanofluids. *J Colloid Interface Sci* 2016;469:17-24. DOI PubMed

46.   Poletayev AD, Mckay IS, Chueh WC, Majumdar A. Continuous electrochemical heat engines. *Energy Environ Sci* 2018;11:2964-71. DOI

47.   Kim JH, Lee JH, Palem RR, Suh MS, Lee HH, Kang TJ. Iron (II/III) perchlorate electrolytes for electrochemically harvesting low-grade thermal energy. *Sci Rep* 2019;9:8706. DOI PubMed PMC

48.   Buckingham MA, Marken F, Aldous L. The thermoelectrochemistry of the aqueous iron(ii)/iron(iii) redox couple: significance of the anion and pH in thermogalvanic thermal-to-electrical energy conversion. *Sustain Energy Fuels* 2018;2:2717-26. DOI

49.   Taheri A, Macfarlane DR, Pozo-gonzalo C, Pringle JM. Application of a water-soluble cobalt redox couple in free-standing cellulose films for thermal energy harvesting. *Electrochim Acta* 2019;297:669-75. DOI

50.   Zhou H, Yamada T, Kimizuka N. Supramolecular thermo-electrochemical cells: enhanced thermoelectric performance by host-guest complexation and salt-induced crystallization. *J Am Chem Soc* 2016;138:10502-7. DOI PubMed

51.   Li X, Liu C, Feng S, Fang NX. Broadband light management with thermochromic hydrogel microparticles for smart windows. *Joule* 2019;3:290-302. DOI

52.   Duan J, Yu B, Liu K, et al. P-N conversion in thermogalvanic cells induced by thermo-sensitive nanogels for body heat harvesting. *Nano Energy* 2019;57:473-9. DOI

53.   Han Y, Zhang J, Hu R, Xu D. High-thermopower polarized electrolytes enabled by methylcellulose for low-grade heat harvesting. *Sci Adv* 2022;8:eabl5318. DOI PubMed PMC

54.   Im H, Moon HG, Lee JS, Chung IY, Kang TJ, Kim YH. Flexible thermocells for utilization of body heat. *Nano Res* 2014;7:443-52. DOI

55.   Wang Z, Li H, Tang Z, et al. Hydrogel electrolytes for flexible aqueous energy storage devices. *Adv Funct Mater* 2018;28:1804560. DOI

56.   Jin L, Greene GW, Macfarlane DR, Pringle JM. Redox-active quasi-solid-state electrolytes for thermal energy harvesting. *ACS*

Energy Lett 2016;1:654-8. DOI

57. Ding T, Zhou Y, Wang X, et al. All-soft and stretchable thermogalvanic gel fabric for antideformity body heat harvesting wearable. *Adv Energy Mater* 2021;11:2102219. DOI

58. Wang XQ, Chan KH, Lu W, et al. Macromolecule conformational shaping for extreme mechanical programming of polymorphic hydrogel fibers. *Nat Commun* 2022;13:3369. DOI PubMed PMC

59. Liu Z, Cheng H, Le Q, et al. Giant thermoelectric properties of ionogels with cationic doping. *Adv Energy Mater* 2022;12:2200858. DOI

60. Agar JN, Mou CY, Lin JL. Single-ion heat of transport in electrolyte solutions: a hydrodynamic theory. *J Phys Chem* 1989;93:2079-82. DOI

61. Eastman ED. Thermodynamics of non-isothermal systems. *J Am Chem Soc* 1926;48:1482-93. DOI

62. Würger A. Thermal non-equilibrium transport in colloids. *Rep Prog Phys* 2010;73:126601. DOI

63. Guthrie G, Wilson JN, Schomaker V. Theory of the thermal diffusion of electrolytes in a clusius column. *J Chem Phys* 1949;17:310-3. DOI

64. Eastman ED. Theory of the soret effect. *J Am Chem Soc* 1928;50:283-91. DOI

65. Marcus Y. Effect of ions on the structure of water: structure making and breaking. *Chem Rev* 2009;109:1346-70. DOI PubMed

66. Kim SL, Hsu J, Yu C. Thermoelectric effects in solid-state polyelectrolytes. *Org Electron* 2018;54:231-6. DOI

67. Wang H, Zhao D, Khan ZU, et al. Ionic thermoelectric figure of merit for charging of supercapacitors. *Adv Electron Mater* 2017;3:1700013. DOI

68. Kim SL, Lin HT, Yu C. Thermally chargeable solid-state supercapacitor. *Adv Energy Mater* 2016;6:1600546. DOI

69. Li L, Hao M, Yang X, et al. Sustainable and flexible hydrovoltaic power generator for wearable sensing electronics. *Nano Energy* 2020;72:104663. DOI

70. Pu S, Liao Y, Chen K, et al. Thermogalvanic hydrogel for synchronous evaporative cooling and low-grade heat energy harvesting. *Nano Lett* 2020;20:3791-7. DOI PubMed

71. Zhao D, Martinelli A, Willfahrt A, et al. Polymer gels with tunable ionic Seebeck coefficient for ultra-sensitive printed thermopiles. *Nat Commun* 2019;10:1093. DOI PubMed PMC

72. Kim B, Hwang JU, Kim E. Chloride transport in conductive polymer films for an n-type thermoelectric platform. *Energy Environ Sci* 2020;13:859-67. DOI

73. Chen Q, Chen B, Xiao S, et al. Giant thermopower of hydrogen ion enhanced by a strong hydrogen bond system. *ACS Appl Mater Interfaces* 2022;14:19304-14. DOI PubMed

74. Haras M, Skotnicki T. Thermoelectricity for IoT - a review. *Nano Energy* 2018;54:461-76. DOI

75. Cheng H, He X, Fan Z, Ouyang J. Flexible quasi-solid state ionogels with remarkable seebeck coefficient and high thermoelectric properties. *Adv Energy Mater* 2019;9:1901085. DOI

76. Stephens GL, Li J, Wild M, et al. An update on Earth's energy balance in light of the latest global observations. *Nat Geosci* 2012;5:691-6. DOI

77. Yin J, Zhou J, Fang S, Guo W. Hydrovoltaic energy on the way. *Joule* 2020;4:1852-5. DOI

78. Zhang Z, Li X, Yin J, et al. Emerging hydrovoltaic technology. *Nat Nanotechnol* 2018;13:1109-19. DOI PubMed

79. Huang Y, Cheng H, Yang C, Yao H, Li C, Qu L. All-region-applicable, continuous power supply of graphene oxide composite. *Energy Environ Sci* 2019;12:1848-56. DOI

80. Cheng H, Huang Y, Zhao F, et al. Spontaneous power source in ambient air of a well-directionally reduced graphene oxide bulk. *Energy Environ Sci* 2018;11:2839-45. DOI

81. Huang Y, Cheng H, Yang C, et al. Interface-mediated hygroelectric generator with an output voltage approaching 1.5 volts. *Nat Commun* 2018;9:4166. DOI PubMed PMC

82. Yin J, Li X, Yu J, Zhang Z, Zhou J, Guo W. Generating electricity by moving a droplet of ionic liquid along graphene. *Nat Nanotechnol* 2014;9:378-83. DOI PubMed

83. Yin J, Zhang Z, Li X, et al. Waving potential in graphene. *Nat Commun* 2014;5:3582. DOI PubMed

84. Cai H, Guo Y, Guo W. Synergistic effect of substrate and ion-containing water in graphene based hydrovoltaic generators. *Nano Energy* 2021;84:105939. DOI

85. Xue G, Xu Y, Ding T, et al. Water-evaporation-induced electricity with nanostructured carbon materials. *Nat Nanotechnol* 2017;12:317-21. DOI PubMed

86. Li J, Liu K, Ding T, Yang P, Duan J, Zhou J. Surface functional modification boosts the output of an evaporation-driven water flow nanogenerator. *Nano Energy* 2019;58:797-802. DOI

87. Liu K, Ding T, Li J, et al. Thermal-electric nanogenerator based on the electrokinetic effect in porous carbon film. *Adv Energy Mater* 2018;8:1702481. DOI

88. Zhao F, Cheng H, Zhang Z, Jiang L, Qu L. Direct power generation from a graphene oxide film under moisture. *Adv Mater* 2015;27:4351-7. DOI PubMed

89. Yang C, Huang Y, Cheng H, Jiang L, Qu L. Rollable, stretchable, and reconfigurable graphene hygroelectric generators. *Adv Mater* 2019;31:e1805705. DOI PubMed

90. Xu T, Ding X, Huang Y, et al. An efficient polymer moist-electric generator. *Energy Environ Sci* 2019;12:972-8. DOI

91. Yang S, Tao X, Chen W, et al. Ionic hydrogel for efficient and scalable moisture-electric generation. *Adv Mater* 2022;34:2200693.

DOI PubMed

92.   Xue J, Zhao F, Hu C, et al. Vapor-activated power generation on conductive polymer. *Adv Funct Mater* 2016;26:8784-92. DOI

93.   Pope M, Swenberg CE. Electronic processes in organic crystals and polymers. Oxford UK: Oxford University Press, 1999.

94.   Ochi S, Kamishima O, Mizusaki J, Kawamura J. Investigation of proton diffusion in Nafion®117 membrane by electrical conductivity and NMR. *Solid State Ion* 2009;180:580-4. DOI

95.   Liu X, Gao H, Ward JE, et al. Power generation from ambient humidity using protein nanowires. *Nature* 2020;578:550-4. DOI PubMed

96.   Gouveia RF, Galembeck F. Electrostatic charging of hydrophilic particles due to water adsorption. *J Am Chem Soc* 2009;131:11381-6. DOI PubMed

97.   Zhang Y, Guo S, Yu ZG, et al. An asymmetric hygroscopic structure for moisture-driven hygro-ionic electricity generation and storage. *Adv Mater* 2022;34:e2201228. DOI PubMed

98.   Zhang Y, Yu Z, Qu H, et al. Self-sustained programmable hygro-electronic interfaces for humidity-regulated hierarchical information encryption and display. *Adv Mater* 2022:2208081. DOI PubMed

99.   Luo Z, Liu C, Fan S. A moisture induced self-charging device for energy harvesting and storage. *Nano Energy* 2019;60:371-6. DOI

100.   Li M, Zong L, Yang W, et al. Biological nanofibrous generator for electricity harvest from moist air flow. *Adv Funct Mater* 2019;29:1901798. DOI

101.   Das SS, Pedireddi VM, Bandopadhyay A, Saha P, Chakraborty S. Electrical power generation from wet textile mediated by spontaneous nanoscale evaporation. *Nano Lett* 2019;19:7191-200. DOI PubMed

102.   Xiao K, Jiang L, Antonietti M. Ion transport in nanofluidic devices for energy harvesting. *Joule* 2019;3:2364-80. DOI

103.   Zhou S, Qiu Z, Strømme M, Xu C. Solar-driven ionic power generation via a film of nanocellulose @ conductive metal-organic framework. *Energy Environ Sci* 2021;14:900-5. DOI

104.   Zhang Y, Sohn A, Chakraborty A, Yu C. Colossal thermo-hydro-electrochemical voltage generation for self-sustainable operation of electronics. *Nat Commun* 2021;12:5269. DOI PubMed PMC